

Increased mTOR activity and metabolic efficiency in mouse and human cells containing the African-centric tumor-predisposing p53 variant Pro47Ser

Keerthana Gnanapradeepan^{1,2}, Julia I-Ju Leu³, Subhasree Basu¹, Thibaut Barnoud¹, Madeline Good¹, Joyce V Lee⁴, William J Quinn⁵, Che-Pei Kung⁶, Rexford Ahima⁷, Joseph A Baur⁵, Kathryn E Wellen⁴, Qin Liu¹, Zachary T Schug¹, Donna L George³, Maureen E Murphy^{1*}

¹Program in Molecular and Cellular Oncogenesis, The Wistar Institute, Philadelphia, United States; ²Graduate Group in Biochemistry and Molecular Biophysics, Perelman School of Medicine, University of Pennsylvania, Philadelphia, United States; ³Department of Genetics, Perelman School of Medicine, University of Pennsylvania, Philadelphia, United States; ⁴Department of Cancer Biology, Perelman School of Medicine, University of Pennsylvania, Philadelphia, United States; ⁵Department of Physiology and Institute for Diabetes, Obesity, and Metabolism, Perelman School of Medicine, University of Pennsylvania, Philadelphia, United States; ⁶Washington University in St. Louis, St Louis, United States; ⁷Division of Endocrinology, Diabetes & Metabolism, Johns Hopkins University School of Medicine, Baltimore, United States

Abstract The Pro47Ser variant of p53 (S47) exists in African-descent populations and is associated with increased cancer risk in humans and mice. Due to impaired repression of the cystine importer *Slc7a11*, S47 cells show increased glutathione (GSH) accumulation compared to cells with wild-type p53. We show that mice containing the S47 variant display increased mTOR activity and oxidative metabolism, as well as larger size, improved metabolic efficiency, and signs of superior fitness. Mechanistically, we show that mTOR and its positive regulator Rheb display increased association in S47 cells; this is due to an altered redox state of GAPDH in S47 cells that inhibits its ability to bind and sequester Rheb. Compounds that decrease glutathione normalize GAPDH-Rheb complexes and mTOR activity in S47 cells. This study reveals a novel layer of regulation of mTOR by p53, and raises the possibility that this variant may have been selected for in early Africa.

*For correspondence: mmurphy@wistar.org

Competing interest: See page 22

Funding: See page 22

Received: 13 February 2020

Accepted: 28 October 2020

Published: 10 November 2020

Reviewing editor: Lydia WS Finley, Memorial Sloan Kettering Cancer Center, United States

© Copyright Gnanapradeepan et al. This article is distributed under the terms of the [Creative Commons Attribution License](#), which permits unrestricted use and redistribution provided that the original author and source are credited.

Introduction

The p53 tumor suppressor protein serves as a master regulator of the cellular response to intrinsic and extrinsic stress. Mutations in the *TP53* gene occur in more than 50% of human cancers, and this gene is well known as the most frequently mutated gene in cancer (*Hollstein et al., 1991*). p53 works to suppress uncontrolled cellular growth and proliferation through various pathways including apoptosis, senescence, cell cycle arrest, and ferroptosis (*Stockwell et al., 2017; Vousden and Prives, 2009*). More recently, a role for p53 in the control of metabolism has emerged. The metabolic functions of p53 include the regulation of mitochondrial function, autophagy, cellular redox

state, and the control of lipid and carbohydrate metabolism; for review see *Berkers et al., 2013*; *Gnanapradeepan et al., 2018*.

As an integral part of its control of metabolism, p53 negatively regulates the activity of mTOR (mammalian target of rapamycin), which is a master regulator of metabolism in the cell. mTOR is a serine-threonine protein kinase that is stimulated by mitogenic signals, and phosphorylates downstream targets that in turn regulate protein synthesis and cell growth (*Ben-Sahra and Manning, 2017*). mTOR exists in two distinct signaling complexes: mTORC1 is primarily responsible for cell growth and protein synthesis, while mTORC2 plays roles in growth factor signaling, cytoskeletal control, and cell spreading (*Liu and Sabatini, 2020*). Not surprisingly, mTOR activity is frequently upregulated in a diverse range of cancers. p53 negatively regulates the mTOR pathway in part through transactivation of the target genes *PTEN*, *TSC2*, *PRKAB1* and *SESN1/SESN2* (*Budanov and Karin, 2008*; *Feng et al., 2005*). The regulation of mTOR by p53 is believed to couple the control of genome integrity with the decision to proliferate (*Hasty et al., 2013*).

TP53 harbors several functionally impactful genetic variants or single-nucleotide polymorphisms (SNPs) (*Basu et al., 2018*; *Jennis et al., 2016*; *Kung et al., 2016*). A naturally occurring SNP in *TP53* exists at codon 47, encoding serine instead of a proline (Pro47Ser, rs1800371, G/A). This variant exists predominantly in African-descent populations, and occurs in roughly 1% of African Americans and 6% of Africans from sub-Saharan Africa (*Murphy et al., 2017*). The S47 variant is associated with increased risk for pre-menopausal breast cancer in African American women (*Murphy et al., 2017*). In a mouse model, the S47 mouse develops markedly increased incidence of spontaneous cancer, particularly hepatocellular carcinoma (*Jennis et al., 2016*). This variant is likewise defective in the regulation of the small subset of p53 target genes that play roles in ferroptosis sensitivity, including the cystine importer *SLC7A11*. As a result, increased levels of cysteine and glutathione (GSH) accumulate in cells from S47 humans and mice (*Jennis et al., 2016*; *Leu et al., 2019*). More recently, we showed that the ferroptotic defect in S47 mice leads to iron accumulation in their livers, spleens, and macrophages. We also showed that the S47 variant is positively associated with markers of iron overload in African Americans (*Singh et al., 2020*).

An emerging paradigm in the cancer literature is that tumor-predisposing genetic variants may paradoxically provide selection benefit to individuals, thus potentially explaining the frequency of these damaging alleles in the population. As an example, women carrying tumor-predisposing mutations in the *BRCA1* gene tend to be physically larger and show increased fertility (*Smith et al., 2012*). Here-in we show that mice carrying a knock-in S47 allele in a pure C57Bl/6 background show increased size, lean content (muscle), and metabolic efficiency, relative to littermate mice with WT p53. We report that mouse and human S47 cells show a significant increase in mTOR activity, due in part to increased mTOR-Rheb binding in S47 cells. We propose that these attributes may have led to a positive selection for this variant in sub-Saharan Africa. Our studies shed further light on the intricate regulation that exists between p53, mTOR activity, and metabolic output, in this case mediated by GSH and the control of cellular redox state.

Results

Higher basal mTOR activity in cells containing the S47 variant

We previously showed that human lymphoblastoid cells (LCLs) that are homozygous for the S47 variant of p53 are impaired for the transcriptional regulation of less than a dozen p53 target genes, compared to cells from individuals from the same family containing WT p53 (*Jennis et al., 2016*). We noted that several of these genes encode proteins that play roles in the negative regulation of mTOR (*Budanov and Karin, 2008*; *Feng et al., 2007*). We confirmed via qRT-PCR that S47 LCLs show modestly decreased expression of the p53 target genes *SESN1* and *PTEN*, and decreased transactivation of *PRKAB1*, relative to WT LCLs following cisplatin treatment (**Figure 1—figure supplement 1A and B**). These findings prompted us to assess basal mTOR activity in WT and S47 LCLs, and in MEFs from WT and S47 mice. To corroborate our findings, we also analyzed tissues from humanized p53 knock-in (Hupki) mice carrying WT and S47 alleles on a pure C57Bl/6 background, which we previously generated and characterized (*Jennis et al., 2016*). Western blot analysis of WT and S47 LCLs, along with multiple clones of WT and S47 MEFs, revealed increased p-S6K1 (Thr389) in S47 cells (**Figure 1A**). Following normalization to total S6K1, this increase ranged between two-

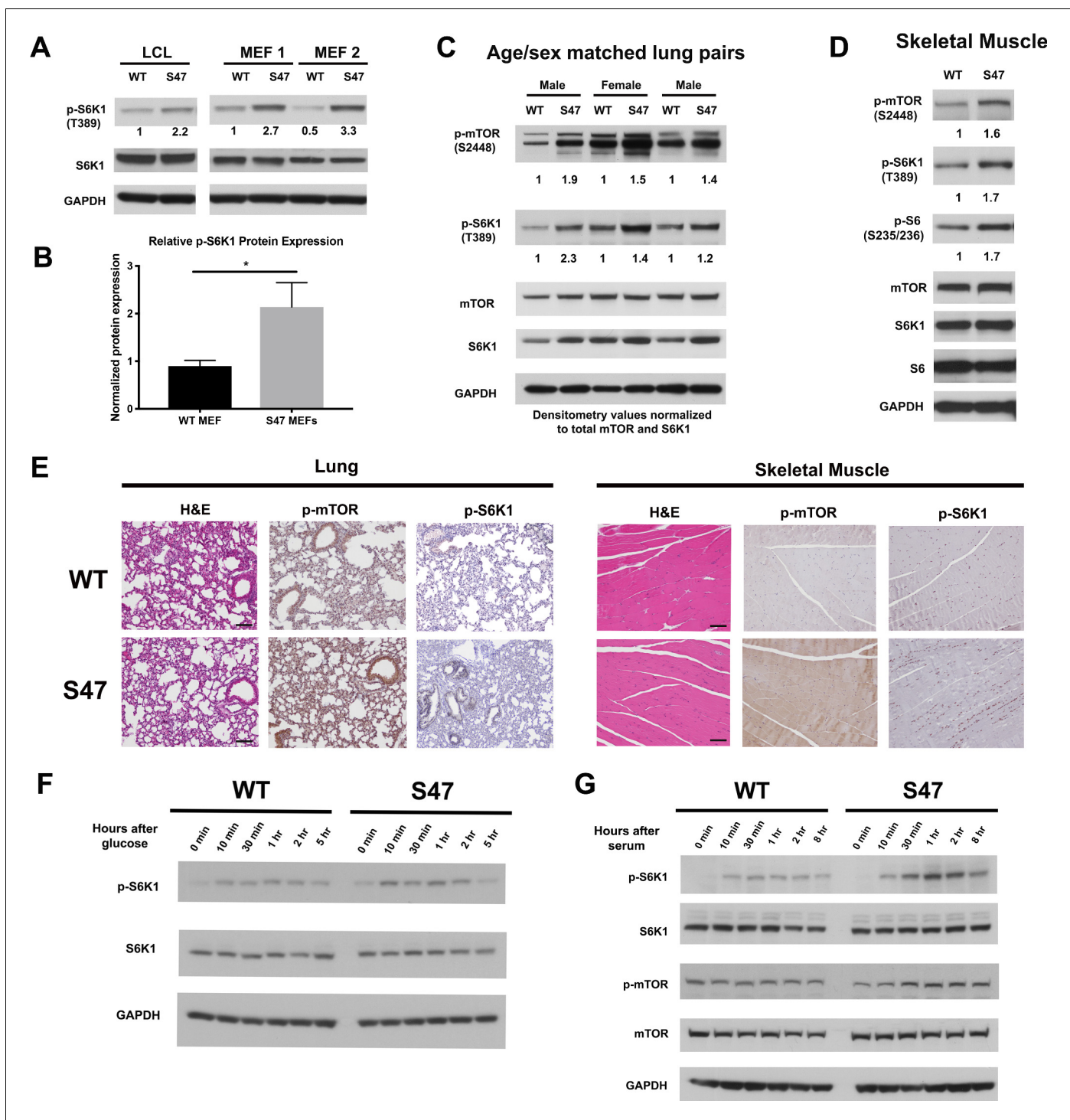


Figure 1. Increased markers of mTOR activity in S47 cells and tissues. (A) Western blot analyses reveal higher phospho-S6K1 expression in S47 LCLs and S47 MEFs; the latter were obtained from two separate embryos per genotype. (B) Densitometry quantification of phospho-S6K1 protein expression in WT and S47 MEFs from four independent experiments; all values normalized to total S6K1. Error bars represent standard error, (*) p value < 0.05. (C) Whole cell lysates were extracted from three WT and three S47 mouse lungs and analyzed by western blot for the proteins indicated. Pairs 1 and 3 are lungs isolated from male mice, pair 2 is lungs isolated from female mice. Densitometry quantification of phospho-S6K1 and phospho-mTOR was performed and normalized to total S6K1 and total mTOR protein expression, respectively. (D) Whole cell lysates were extracted from WT and S47 mouse skeletal muscle and analyzed as described above. Densitometry quantification of phospho-S6, phospho-S6K1, phospho-mTOR was performed and normalized to total S6, total S6K1 and total mTOR protein expression, respectively. (E) Immunohistochemical analysis of hematoxylin and eosin (H and E), phospho-mTOR and phospho-S6K1 in WT and S47 mouse lung and skeletal tissue. Data are representative of n = 4 mice per genotype. Scale Figure 1 continued on next page

Figure 1 continued

bar represents 100 μm . (F) WT and S47 MEFs were grown in glucose-free media for 16 hr, then in media containing 4.5 g/L glucose. Samples were collected at indicated time points and analyzed by western blot for p-S6K1, total S6K1, and GAPDH. (G) WT and S47 MEFs were cultured in media containing 0.1% FBS for 16 hr, followed by media containing 10% serum and samples were collected at indicated time points. Cell lysates were extracted from samples and subjected to western blot analysis for the proteins indicated.

The online version of this article includes the following figure supplement(s) for figure 1:

Figure supplement 1. Altered metabolic markers in S47 cells and tissues.

and threefold (**Figure 1B**). We next compared mTOR activity in age- and sex-matched pairs of lung and muscle tissue from WT and S47 mice; we did this because mTOR activity is influenced by age and gender, and there is increased mTOR activity in female and older mice (*Baar et al., 2016*). We found increased levels of p-S6K1 (T389) and p-mTOR (Ser2448) in S47 lung and skeletal muscle, relative to WT tissues (**Figure 1C and D**). Immunohistochemical analysis of tissues from multiple age- and sex-matched WT and S47 mice confirmed these findings (**Figure 1E**). Interestingly, increased mTOR activity was not seen in all tissues of the S47 mouse (**Figure 1—figure supplement 1C**), and lung and skeletal muscle were the most consistently different between WT and S47. We also did not detect significant differences in p-AKT (Ser473) in WT and S47 lung tissue, suggesting that mTORC1 and not mTORC2 is likely responsible for the observed differences in mTOR activity (**Figure 1—figure supplement 1D**).

We next sought to test the kinetics of mTOR activation in WT and S47 cells by subjecting early passage WT and S47 MEFs to nutrient deprivation, followed by monitoring of mTOR activation markers after nutrient restoration using antisera to p-S6K1 and p-mTOR. Glucose deprivation experiments revealed consistent albeit modest increases in p-S6K1 following glucose refeed in S47 MEFs, compared to WT (**Figure 1F**). Serum deprivation experiments revealed more pronounced results. For serum deprivation, we subjected three independent cultures each of WT and S47 MEFs to 0.1% serum for 16 hr, followed by 10% serum, after which total and phospho -S6K1 and -mTOR were monitored in a time course. S47 cells consistently showed increased induction of markers of mTOR activation after serum re-feed compared to WT cells (**Figure 1G**). We next performed amino acid deprivation experiments; these likewise showed increased response in S47 cells (**Figure 1—figure supplement 1E**). Combined densitometry results from all forms of nutrient deprivation revealed an approximately two- to threefold increase in p-S6K1 in S47 cells following nutrient restoration at 30 or 60 min (**Figure 1—figure supplement 1F**).

Given that mTOR plays a role in autophagy inhibition (*Jung et al., 2010; White et al., 2011*), we wondered whether basal autophagy or autophagic flux might be decreased in S47 cells. We were unable to see any differences in the steady state levels of LC3B or the autophagy adaptor protein p62^{SQSTM1} in WT and S47 MEFs or tissues, either at steady state (**Figure 1—figure supplement 1G**) or following HBSS treatment to induce autophagy (**Figure 1—figure supplement 1H**). Likewise, we failed to see differences in autophagic flux (conversion of LC3-I to LC3-II when the lysosome is inhibited (**Figure 1—figure supplement 1I**)) between WT and S47 cells, or in cell viability after HBSS treatment (**Figure 1—figure supplement 1J**). Therefore, while markers of mTOR activity are clearly increased in S47 cells and tissues, this does not appear to be accompanied by alterations of basal or induced autophagy.

Enhanced mitochondrial function and glycolysis in S47 cells

To determine the functional consequences of the increased markers of mTOR activity in S47 cells, we used a Seahorse BioAnalyzer to assess the oxygen consumption rate (OCR), as well as basal and compensatory glycolytic rate in WT and S47 MEFs and LCLs. Seahorse analyses revealed that S47 LCLs show increased OCR under stressed conditions compared to WT (**Figure 2A**). These analyses also revealed that human S47 LCLs and mouse S47 MEFs show increased basal and compensatory glycolysis, compared to WT cells (**Figure 2B and C**). We next assessed glucose and glutamine consumption using a Yellow Springs Instrument (YSI) Analyzer. These analyses revealed that S47 LCLs and MEFs show significantly increased consumption of glucose and glutamine, along with increased production of lactate and glutamate, compared to WT cells (**Figure 2D and E**); again, multiple independent MEF lines were analyzed. Interestingly, LCLs from individuals heterozygous for the S47

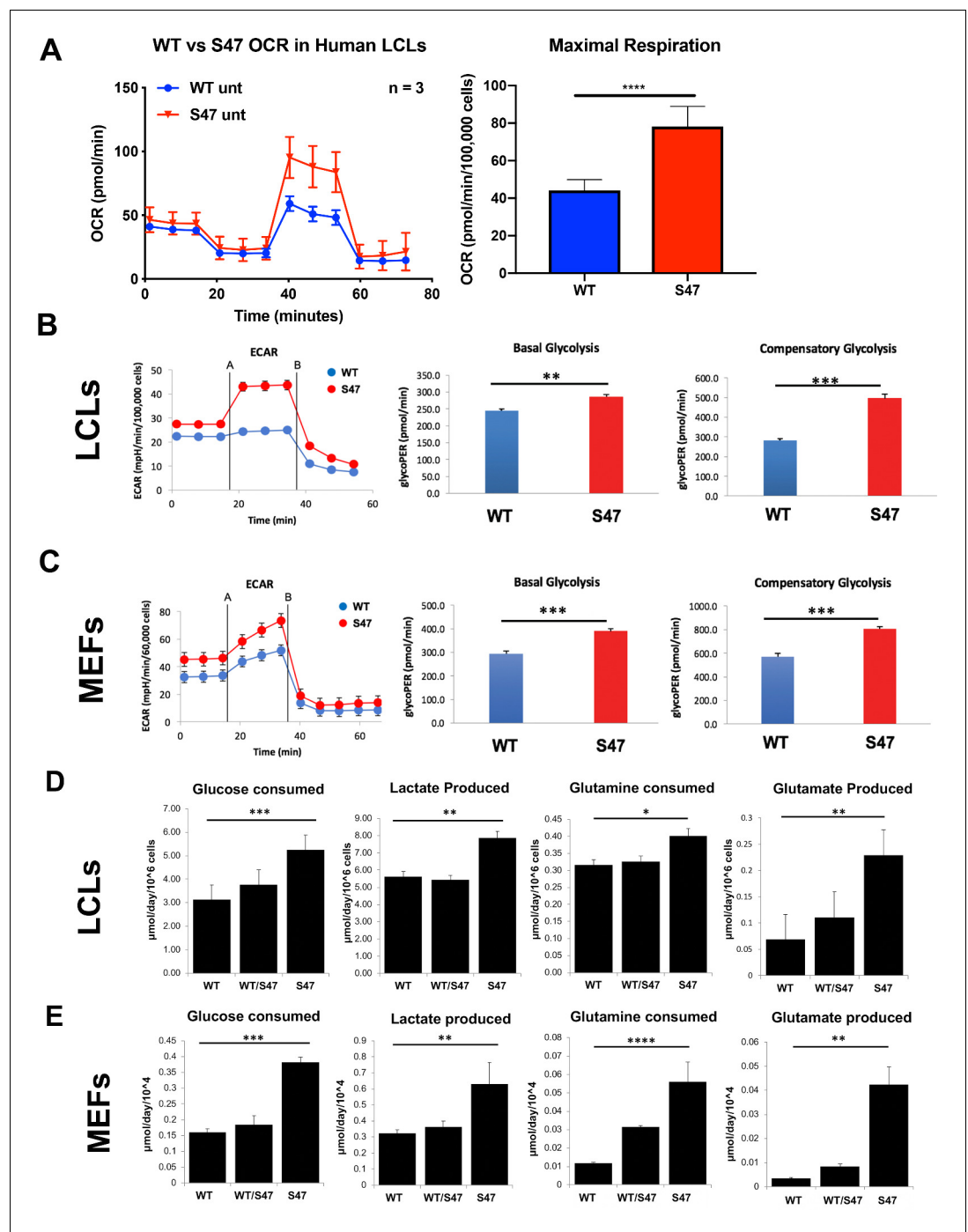


Figure 2. Increased metabolism in S47 cells compared to WT cells. (A) Oxygen consumption rates (OCR) in WT and S47 LCLs were assessed using the Seahorse XF Mito Stress Test. OCR was measured first in basal conditions, and following injection of oligomycin, FCCP and rotenone/antimycin. The bar graph depicts maximal OCR after FCCP injection at ~40 min timepoint; data are representative of three independent experiments performed with at least six technical replicates, presented as mean \pm SD. (B–C) Basal and compensatory glycolysis in WT and S47 LCLs (B) and MEFs (C) were assessed using the Seahorse Glycolytic Rate Assay. Basal glycolysis is first measured, followed by treatment of cells with rotenone/antimycin and 2-deoxy-D-glucose (2-DG). The bar graph depicts basal glycolysis at ~1 min timepoint and compensatory glycolysis after antimycin/rotenone injection at ~22 min timepoint; data are representative of three independent experiments performed with at least 10 technical replicates. Bar graphs are presented as mean \pm SD. (D–E) Consumption of glucose and glutamine from media and production of lactate and glutamate were analyzed from homozygous WT, heterozygous WT/S47 and

Figure 2 continued on next page

Figure 2 continued

homozygous S47 human LCLs (D) and primary MEFs (E) using a YSI-7100 Bioanalyzer. Means and SEM are shown (n = 5).

The online version of this article includes the following source data and figure supplement(s) for figure 2:

Figure supplement 1. Increased metabolism in S47 MEFs but no differences in mitochondrial content in WT and S47 cells.

Figure supplement 1—source data 1. Metabolomics source data.

variant (S47/WT), and MEFs from S47/WT mice, showed values typically intermediate between homozygous WT and S47 cells (**Figure 2D and E**). We next performed metabolic flux analyses in WT and S47 cells using ^{13}C -labeled glucose. Analysis of $^{13}\text{C}_6$ -glucose tracing in WT and S47 MEFs provided evidence for a higher contribution of glucose carbon into the TCA cycle in S47 cells compared to WT cells, as evidenced by increased labeling of citrate, malate, aspartate, and glutamate in S47 MEFs (**Figure 2—figure supplement 1A–D**). We reasoned that one possibility for the increased metabolism in S47 cells might be due to increased mitochondrial content, which is regulated by mTOR (**Morita et al., 2013**). However, MitoTracker analyses and western blotting for mitochondrial proteins revealed no obvious increase in mitochondrial content in S47 cells (**Figure 2—figure supplement 1E and F**). We find no evidence that S47 LCLs and MEFs proliferate more quickly than WT cells (**Jennis et al., 2016**); this raises the possibility that this increased nutrient consumption may be used for biomass instead of proliferation.

Because mTOR is known to regulate mitochondrial function (**Morita et al., 2013; Schieke et al., 2006; Ye et al., 2012**), we next assessed the impact of mTOR inhibitors on mitochondrial function in WT and S47 cells. Seahorse analysis of WT and S47 LCLs revealed that S47 cells are less susceptible to inhibition of oxygen consumption rate and maximal respiration by the mTOR inhibitors rapamycin (**Figure 3A and B**) and Torin1 (**Figure 3C and D**). This finding was not due to altered efficacy of each inhibitor, as evidenced by similar decreases in p-mTOR and p-S6 in WT and S47 cells following treatment with rapamycin (**Figure 3—figure supplement 1A**) and Torin1 (**Figure 3E**), and by the finding that very high concentrations of Torin1 were able to inhibit oxygen consumption equally well in both WT and S47 cells (**Figure 3—figure supplement 1B**). These data support the possibility of an S47 dependent, but mTOR-independent, effect on OCR as well.

Increased mTOR activity in S47 is due to increased mTOR-Rheb interaction

We next sought to identify the mechanism underlying increased mTOR activity in S47 cells. Unfortunately, although we identified decreased mRNA levels of some mTOR regulators in S47 cells, we found no evidence for significant differences at the protein level of any p53-regulated mTOR regulators in steady state MEFs (**Figure 4—figure supplement 1A**) or following treatment with Nutlin to induce p53 (**Figure 4—figure supplement 1B**). Therefore, we turned to a key regulator of mTOR activity, the small GTPase Rheb, which binds and activates mTOR (**Long et al., 2005**). We monitored the mTOR-Rheb association in WT and S47 MEFs using the technique of proximity ligation assay (PLA), which quantitatively detects protein-protein interactions. PLA experiments revealed that there were consistently increased mTOR-Rheb complexes in S47 cells, compared to WT; this was true in multiple replicates, in multiple MEF clones, and using single antibody controls that showed no signal (**Figure 4A**). Quantification of multiple experiments revealed an approximately two-fold increase in mTOR-Rheb complexes in S47 cells compared to WT (**Figure 4B**), which is consistent with all of our analyses of mTOR activity.

One regulator of the mTOR-Rheb interaction is the cytosolic enzyme GAPDH. This enzyme binds to Rheb and sequesters it from mTOR in cultured cells, in a manner that is regulated by glucose levels (**Lee et al., 2009**). First, we confirmed that the interaction between Rheb and GAPDH is detectable in the skeletal muscle of mice using IP-western, and moreover that this interaction is regulated by glucose (**Figure 4—figure supplement 1C**). Next, we performed immunoprecipitation (IP)-western of Rheb in skeletal muscle extracts from WT and S47 mice; we found that there was increased mTOR, and significantly decreased GAPDH, in Rheb IPs from S47 skeletal muscle compared to WT (**Figure 4C**). The combined data from three independent IPs of Rheb in WT and S47 skeletal muscle

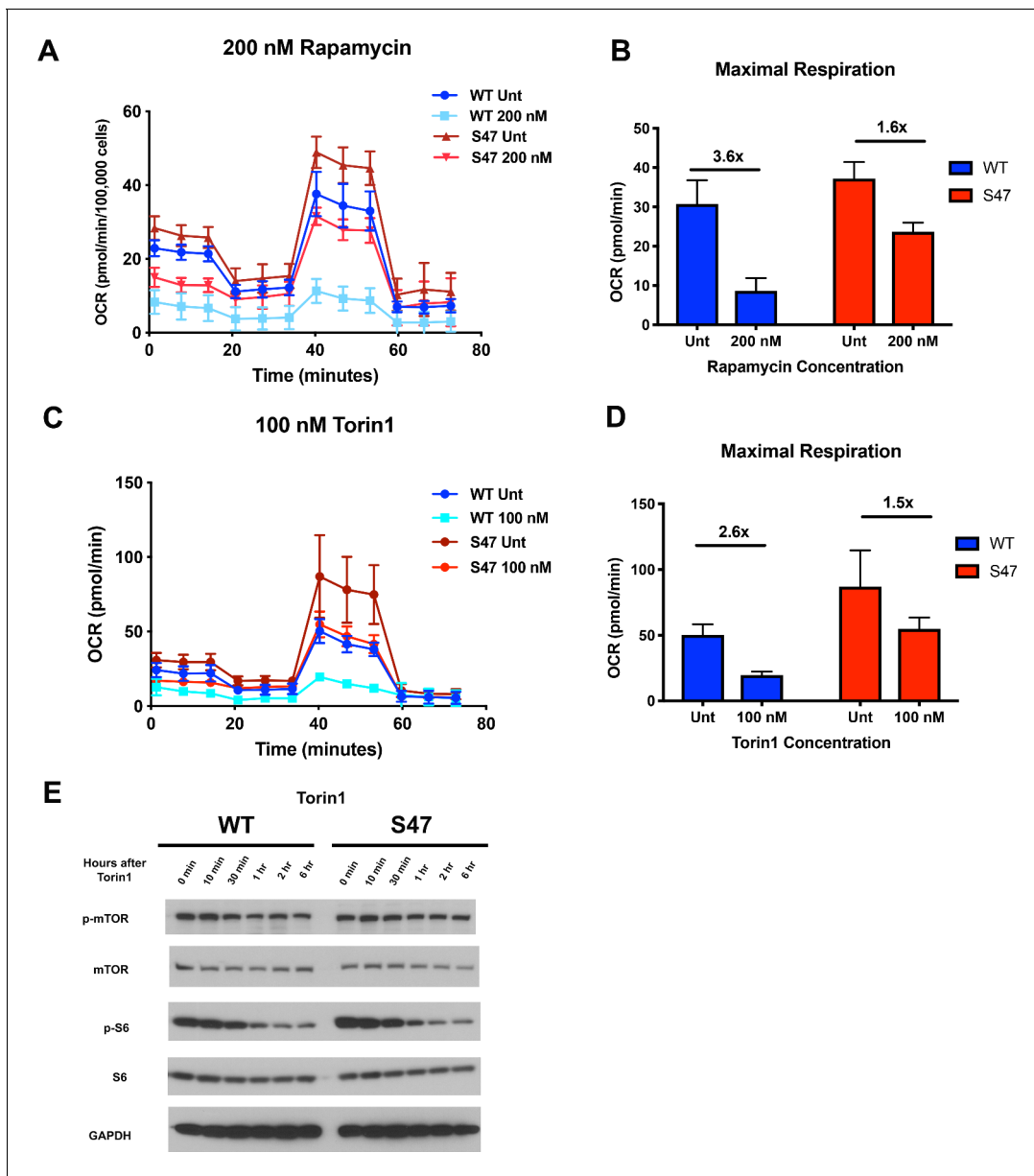


Figure 3. S47 mitochondria show decreased sensitivity to mTOR inhibition. (A) Oxygen consumption rate (OCR) as measured by the Seahorse XF Mito Stress Test in WT and S47 LCLs treated with 200 nM of rapamycin for 24 hr. (B) Bar graph depicts maximal OCR after FCCP injection at ~40 min timepoint; fold changes between rapamycin treated and untreated samples are shown. Data are representative of two independent experiments performed with at least 10 technical replicates. (C) OCR as measured by the Seahorse XF Mito Stress Test in WT and S47 LCLs treated with 100 nM of Torin1 for 24 hr. (D) Bar graph depicts maximal OCR after FCCP injection at ~40 min timepoint; fold changes between Torin1 treated and untreated samples are shown. Data are representative of two independent experiments performed with at least eight technical replicates. (E) WT and S47 LCLs were treated with 100 nM of Torin1, harvested at indicated time points after treatment and analyzed for the shown mTOR markers via western blot. The online version of this article includes the following figure supplement(s) for figure 3:

Figure supplement 1. Attenuated response to mTOR inhibition in S47 cells.

revealed an approximately twofold decrease in the amount of GAPDH co-precipitating with Rheb in S47 skeletal muscle compared to WT ($p < 0.05$, **Figure 4D**). In contrast, there were no differences in the levels of mTOR, Rheb and GAPDH in these extracts (**Figure 4C – WCL**, **Figure 4—figure supplement 1D**). Consistent with our IP-western findings, PLA analyses corroborated that the GAPDH-Rheb association is markedly decreased in S47 MEFs relative to WT MEFs (**Figure 4A**). Confocal microscopy analyses revealed no significant differences in the cellular localization of Rheb at the

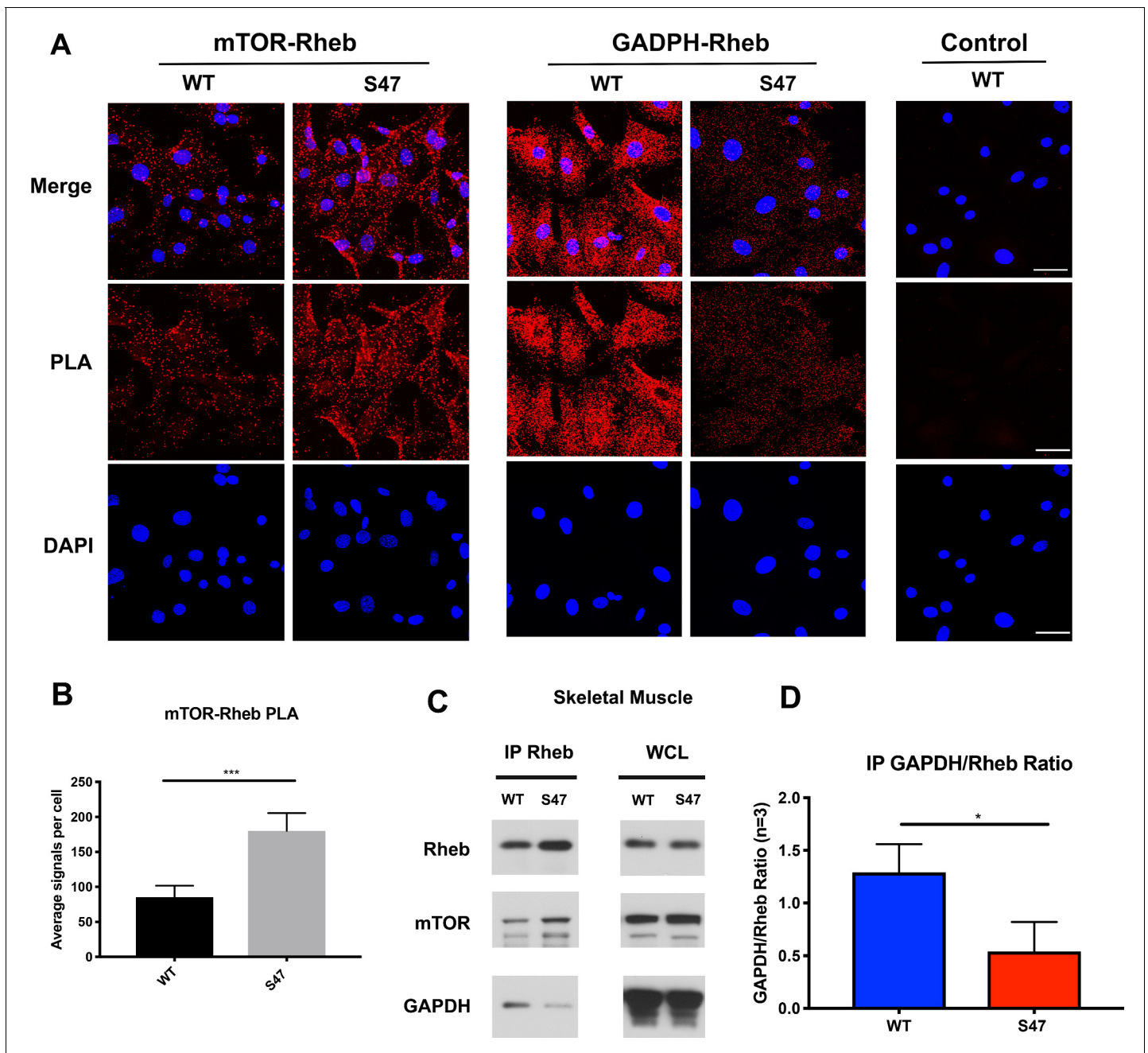


Figure 4. Increased mTOR-Rheb binding in S47 cells is due to decreased GAPDH-Rheb binding. (A–B) An in situ proximity ligation assay (PLA) was performed in WT and S47 MEFs. Each red dot represents an interaction between mTOR-Rheb or GAPDH-Rheb as indicated; scale bar represents 50 μm . The samples were counterstained with DAPI to detect nuclei. Cells stained in the absence of one primary antibody were used as a negative control. (B) Quantification of the mTOR-Rheb interactions, measured as the average number of PLA signals per nuclei. Data were quantified by counting the number of cells in five random fields per experimental condition. (***) p-value < 0.001, Student's t-test. (C) Lysates extracted from WT and S47 skeletal tissue were immunoprecipitated with anti-Rheb. The amount of co-precipitating mTOR and GAPDH, as well as immunoprecipitated Rheb, were assessed by western blot. Whole cell lysate (WCL) is shown on the right. (D) Quantification of the amount of GAPDH bound to Rheb, divided by total Rheb pulled down, in WT and S47 skeletal tissue, n = 3 independent experiments, (*) p-value < 0.05.

The online version of this article includes the following figure supplement(s) for figure 4:

Figure supplement 1. No differences in the level of mTOR regulators in WT and S47 cells.

lysosome, as assessed by LAMP1 localization, nor were there any differences in TSC2 localization at the lysosome in WT and S47 MEFs (**Figure 4—figure supplement 1E**). The combined data support the premise that the increased mTOR activity in S47 cells may be due to increased Rheb-mTOR association, caused by a decreased association of Rheb with GAPDH. We sought to test this hypothesis, and identify the underlying mechanism.

GAPDH is a multi-functional enzyme that is known to be sensitive to redox status (**Brandes et al., 2009; Chernorizov et al., 2010**). We hypothesized that the increased glutathione (GSH) levels in S47 cells (**Leu et al., 2019**) might alter the redox state of GAPDH and impact its ability to bind to Rheb. We first verified that lung tissue and skeletal muscle from S47 mice possess increased GSH compared to WT tissues, as assessed by an increased ratio of reduced versus oxidized glutathione (GSH:GSSG) (**Figure 5A**). We then validated that the GSH alkylating agent diethylmaleate (DEM) could successfully decrease the level of GSH, and the GSH/GSSG ratio, in these cells (**Figure 5A**); these findings are consistent with previously published findings by our group (**Leu et al., 2019**). Notably, DEM treatment of immortalized S47 MEFs (iMEFs) caused a dramatic decrease in markers of mTOR activity (p-mTOR and p-S6K1), showing that modulation of GSH, even for as little as five hours, can impact mTOR activity (**Figure 5B**). Moreover, we found that the impact of DEM on mTOR activity was enhanced by the addition of glutamate, which decreases cystine import through system Xc(-), leading to decreased level of GSH (**Figure 5B**).

We next sought to test the hypothesis that the redox state of GAPDH was altered in WT and S47 cells. Toward this end, we employed cross-linking experiments using the cysteinyl cross-linking agent bismaleimidohexane (BMH), which cross-links cysteine residues within 13 Å by covalently conjugating free (reduced) sulfhydryl groups (**Green et al., 2001**). We treated freshly isolated lung and skeletal muscle lysates from WT and S47 mice, and from immortalized WT and S47 MEFs (iMEFs), with BMH. Cysteinyl-crosslinked proteins were resolved on SDS-PAGE gels and compared to untreated extracts. Notably, we found consistent differences in GAPDH cross-linking patterns in S47 samples compared to WT, as evidenced by altered mobility of GAPDH on SDS-PAGE of BMH-treated samples (**Figure 5C**). Moreover, the altered mobility of GAPDH in S47 cells could be reversed following glutathione depletion by DEM treatment (**Figure 5C**) or by the compound BSO (buthionine sulfoximine; **Figure 5—figure supplement 1A**) which inhibits GSH biosynthesis. Treatment with the compound erastin, which inhibits the system Xc(-) cystine transporter and decreases GSH, also led to altered mobility of GAPDH in S47 and WT cells (**Figure 5—figure supplement 1B**). We next tested the impact of modulating GSH on the interaction between Rheb and GAPDH in WT and S47 cells using both IP-western and PLA. By IP-western we found that supplementation of culture media with exogenous GSH decreased the Rheb-GAPDH interaction in WT cells; conversely, depleting free GSH using either BSO or DEM increased the Rheb-GAPDH interaction in S47 cells (**Figure 5D**). These findings were corroborated using PLA, which revealed that depleting GSH using either DEM or BSO completely restores GAPDH-Rheb complex formation and mTOR-Rheb complex formation in S47 cells, to levels equivalent to WT cells (**Figure 5E and F; Figure 5—figure supplement 1C**). The combined data support the conclusion that the increased GSH pool in S47 cells affects the status of reactive cysteines in GAPDH, and the ability of this protein to bind and sequester Rheb, thereby leading to increased Rheb-mTOR interaction and increased mTOR activity in S47 cells.

Enhanced metabolic efficiency of S47 mice

mTOR is known to regulate body mass and muscle regeneration (**Laplante and Sabatini, 2012; Yoon, 2017**). We therefore next assessed body weight and fat/lean content in age-matched male mice of WT and S47 genotypes. We also tracked body weight with age of multiple male and female sibling littermate mice of WT/WT, WT/S47, and S47/S47 genotypes in our colony. S47 mice showed significantly increased weight with time, compared to WT/WT and WT/S47 sibling littermates (**Figure 6—figure supplement 1A**). Body composition analysis using nuclear magnetic resonance revealed that S47 mice had significantly increased fat and lean content, compared to WT mice (**Figure 6A; Figure 6—figure supplement 1B**). We next analyzed the metabolic activities of WT and S47 mice using a comprehensive lab animal monitoring system (CLAMS) over the course of 48 hr. In this analysis, S47 mice showed comparable locomotor activity to WT mice but reduced food intake, oxygen consumption, and heat production (**Figure 6B**). These CLAMS data suggested that S47 mice might possess enhanced metabolic efficiency compared to WT mice, and prompted us to assess the response of WT and S47 mice to exercise challenge.

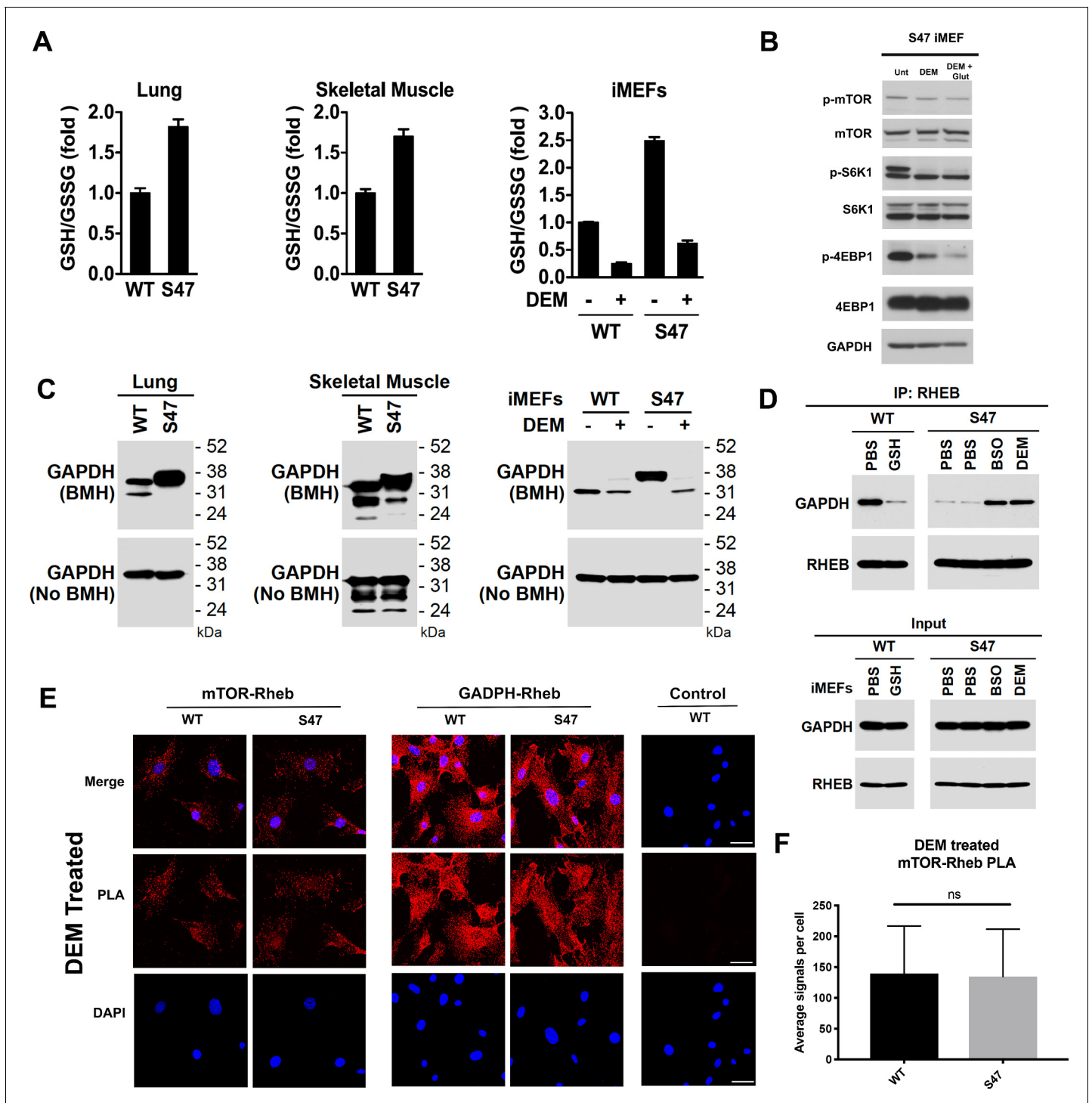


Figure 5. Increased glutathione drives decreased GAPDH-Rheb binding in S47 cells. (A) WT and S47 lung (left) and skeletal muscle (center) were assessed for GSH/GSSG ratio (mean \pm SD, $n = 3$). WT and S47 immortalized MEFs (iMEFs), either untreated or treated with 50 μ M DEM for 5 hr, were analyzed for GSH/GSSG ratio (mean \pm SD, $n = 4$). (B) WT and S47 iMEFs were untreated or treated with 50 μ M of DEM or 50 μ M of DEM + 0.5 mM glutamate for 5 hr and protein lysates were analyzed by western blot for indicated mTOR markers. (C) Whole cell lysates were extracted from WT and S47 mouse lung (left) and skeletal (center) tissue. Proteins were cross-linked with BMH, resolved by SDS/PAGE, and detected by western blotting with a GAPDH specific antibody (Top). Untreated protein lysates were analyzed by western blot analysis for total GAPDH (Bottom). WT and S47 iMEFs were treated with 50 μ M of DEM for 5 hr and protein lysates were analyzed as described (right). (D) WT cells were treated with PBS or 3 mM GSH for 24 hr. S47 cells were treated with PBS for 24 hr, PBS for 5 hr, 100 μ M BSO for 24 hr, or 50 μ M DEM for 5 hr. IP of the lysates with anti-Rheb followed by western analysis for associated GAPDH and Rheb (top panel). The same lysates were analyzed by western blotting for GAPDH and Rheb (bottom panel). *Figure 5 continued on next page*

Figure 5 continued

panel). (E–F) Proximity ligation analysis (PLA) was performed in WT and S47 MEFs treated with 50 μ M of DEM for 5 hr and analyzed as described in **Figure 4A–B**. Scale bar is 30 μ m.

The online version of this article includes the following figure supplement(s) for figure 5:

Figure supplement 1. Glutathione depletion by BSO alters GAPDH cross-linking and the GAPDH-Rheb interaction.

We subjected WT and S47 mice to treadmill exercise with increasing intensity over time. For this analysis, we studied eight age-matched male mice of each genotype during a 50 min forced exercise at increasing speed and slope. During this time course, oxygen consumption and serum metabolites were quantified. Consistent with our CLAMs experiment, S47 mice started with lower basal VO_2 and exhibited generally lower VO_2 for the work being performed; however, as they approached the final, most strenuous point of the exercise, the VO_2 values in WT and S47 converged, so the VO_2 range for S47 mice was significantly greater than WT mice (**Figure 6C–E**). Analysis of serum metabolites and proteins before and after exercise revealed decreased lactate dehydrogenase (LDH) levels in the sera of S47 mice, which is indicative of decreased muscle damage in S47 mice compared to WT (**Figure 6F**). Additionally, we found that Ki-67 staining in S47 skeletal muscle was consistently increased relative to WT muscle, suggesting an enhanced ability for S47 muscle to recover (**Figure 6—figure supplement 1C**). In these tissues, we found no differences in p53 level or markers of mitochondrial content (**Figure 6—figure supplement 1D and E**), nor were there other differences in other serum metabolites between WT and S47 mice (**Figure 6—figure supplement 1F**). These exercise data, like the CLAMs data, point to increased metabolic efficiency in S47 mice relative to WT mice. To address this further, we analyzed a small cohort of WT and S47 mice on a continuous strenuous treadmill run. Although the numbers are small, we found that three out of four WT mice failed to complete a 60 min strenuous run, while three out of four S47 successfully completed this run (**Figure 6—figure supplement 1G**).

Discussion

In this study, we report that cells and mice with the S47 variant of p53 have increased mTOR activity and evidence for increased metabolic efficiency. The animals also display increased mass and signs of superior fitness. Our data support the premise that the enhanced mTOR activity is due, at least in part, to the higher levels of GSH in S47 cells and tissues. The increased GSH results in impaired ability of the redox sensitive protein GAPDH to bind to Rheb. This leads to greater mTOR-Rheb binding, resulting in increased mTOR activity in S47 cells and tissues. These data indicate that, along with pH (**Walton et al., 2018**), cellular redox status can also regulate mTOR activity, in a manner controlled by p53. We show that oxidative metabolism in S47 cells is less sensitive to mTOR inhibitors, thus tying these two phenotypes together; this is not surprising, as a link between mTOR and a number of cellular metabolic processes is well known (**Morita et al., 2013; Schieke et al., 2006**).

We see evidence for increased mTOR activity only in certain tissues of the S47 mouse, so the metabolic impact of this genetic variant appears to be influenced by tissue type and cellular environment. At present, we do not know if this tissue specificity is due to differences in GSH level, or to altered mTOR-Rheb or GAPDH-Rheb interactions in different tissues, or to other parameters. We also see evidence for some unexpected findings regarding the increase in mTOR activity in S47 cells: given that mTOR negatively regulates autophagy (**Jung et al., 2010**), we expected to see differences in steady state autophagy or autophagic flux in WT and S47 cells, but we found no evidence for this. This finding may be due to the rather complex relationship between mTOR and autophagy (**Jung et al., 2010; White et al., 2011**), and/or that other signaling pathways regulate autophagy aside from mTOR, including the PI3K pathway, GTPases, and calcium (**Yang et al., 2005**).

The increased lean content in S47 mice likely contributes to the increased fitness observed in these mice. Human studies have shown that mTOR activation is crucial for human muscle protein synthesis (**Dickinson and Rasmussen, 2011**). Treatment with the well-studied mTOR inhibitor rapamycin blocks the effects of amino acid ingestion on mTOR activity and leads to decreased protein synthesis in human skeletal muscle (**Dickinson and Rasmussen, 2011; Drummond et al., 2009**). Additionally, mTOR signaling driven through IGF-1 plays a key role in promoting muscle hypertrophy

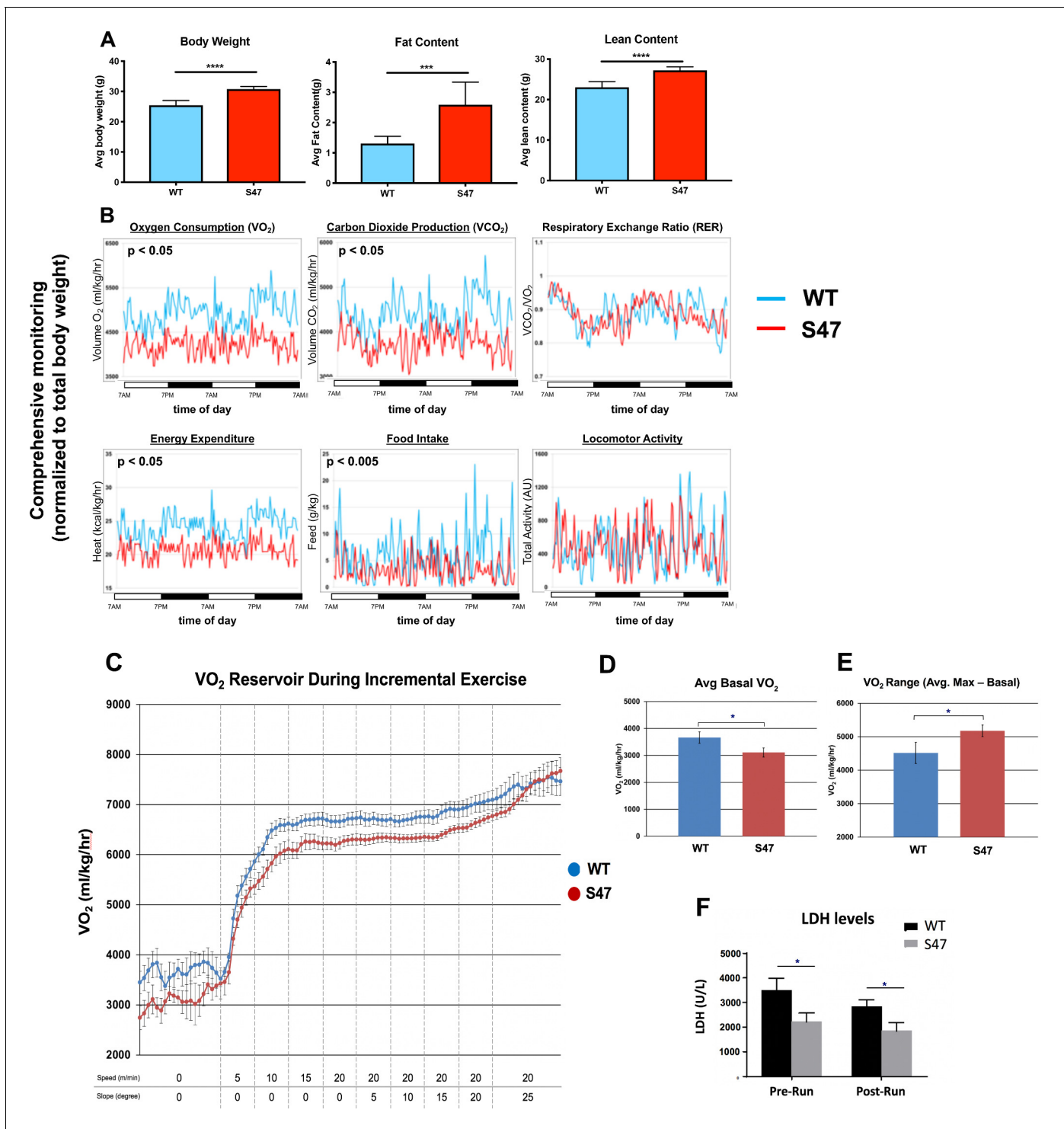


Figure 6. Increased size and improved metabolic efficiency in S47 mice. (A) Nuclear magnetic resonance (NMR) studies revealed S47 mice have increased body weight, increased fat content and increased lean content, $n = 7$ WT mice, $n = 8$ S47 mice. (***) p -value < 0.001, (****) p -value < 0.0001. Bar graphs are presented as mean \pm SD. (B) Changes in metabolic parameters for WT mice (blue) and S47 mice (red) were determined by using the Comprehensive Lab Animal Monitoring System for 48 hr. Parameters assessed includes oxygen consumption, carbon dioxide production, respiratory exchange rate, energy expenditure, total food intake, and locomotor activity. The data are representative of five 6-week old male mice per genotype and are normalized to total body weight. (C) WT and S47 mice ($n = 6-7$) were subjected to a treadmill study of increasing intensity over time. Oxygen consumption (VO₂) is normalized to body mass. (D) Mean basal VO₂ in WT and S47 mice. (E) VO₂ range in WT and S47 mice determined by subtracting the mean basal VO₂ from the VO₂ max, obtained during the most strenuous point of exercise at the tail end of the treadmill study. (F) Lactate

Figure 6 continued on next page

Figure 6 continued

dehydrogenase (LDH) levels measured in the serum of WT and S47 mice obtained before and after the treadmill study. (*) p-value<0.05, Student's t-test.

The online version of this article includes the following source data and figure supplement(s) for figure 6:

Source data 1. Metabolic efficiency source data 1.

Source data 2. Metabolic efficiency source data 2.

Source data 3. Metabolic efficiency source data 3.

Figure supplement 1. Serum metabolites and protein markers pre- and post- exercise.

(Coleman et al., 1995; Musarò et al., 2001; Vandenburg et al., 1991). One caveat of this study, however, is that we do not directly demonstrate that the increased mTOR activity in S47 mice is causing their increased lean content or superior performance on treadmill assays. Transient treatment with mTOR inhibitors elicits highly complex and often contrasting effects on energy expenditure and treadmill performance, likely due to the existence of feedback loops and the effect of inhibitors on multiple organ systems in the mouse. As just two examples: rapamycin has shown contrasting effects on energy expenditure in animals, depending on how long mice are treated (Fang et al., 2013); similarly, treatment of mice with rapamycin has shown limited impact on treadmill endurance, despite causing decreased expression of genes involved in mitochondrial biogenesis and oxidative phosphorylation in the muscle (Ye et al., 2013). Possibly, the most consistent findings in the literature reflect the general consensus that mTORC1 is involved in mechanisms that drive increased muscle mass (Goodman, 2019) and that heightened mTOR activity leads to enhanced muscle recovery after exercise (Song et al., 2017; Yoon, 2017). It remains to be tested if these are the pathways affected in S47 mice.

We hypothesize that the more efficient metabolism and enhanced fitness provided by the S47 variant may have once provided carriers with a bio-energetic advantage in Sub-Saharan western Africa, where this variant is most common. For example, those carrying the S47 SNP may have possessed superior athletic prowess and/or ability to withstand famine (see model, Figure 7). This metabolic advantage may explain the high frequency of this genetic variant in sub-Saharan Africa, despite the fact that it predisposes individuals to cancer later in life. Another positive selection for this variant in Africa may include an improved ability to withstand malaria infection: we recently reported that the S47 variant alters the immune micro-environment in mice and confers improved response to the malaria toxin hemozoin (Singh et al., 2020).

Our findings provide further support for the growing premise that some tumor suppressor genetic variants may provide evolutionary selection benefit (Vicens and Posada, 2018). For example, women who carry the BRCA1/2 mutation exhibit increased size and enhanced fertility when compared to controls (Smith et al., 2012). Similarly, people with Li Fraumeni syndrome who inherit germline mutations in TP53, as well as mice with tumor-derived germline mutations in Tp53, demonstrate increased fitness endurance (Wang et al., 2013); however, this is due to increased mitochondrial content, which we do not see in S47 cells. A common genetic variant in TP53 at codon 72, encoding proline at amino acid 72, confers increased longevity while conversely causing increased cancer risk (Zhao et al., 2018). In contrast, the arginine 72 variant of p53 induces increased expression of LIF, which improves fecundity (Kang et al., 2009). The take home message from all these studies is that the diverse roles of tumor suppressor proteins like p53 in metabolism, fertility, and fitness may allow for positive selection for certain variants, even at the expense of increased cancer risk. In mice, this increased cancer risk occurs quite late in life, well past reproductive selection (12–18 months). More needs to be done to analyze cancer risk in S47 humans. A more comprehensive understanding of the function of tumor suppressor genetic variants, including the S47 SNP, will enable improved understanding of cancer risk, along with superior personalized medicine approaches, with the ultimate goal of improving clinical outcomes and survival of people who carry this variant.

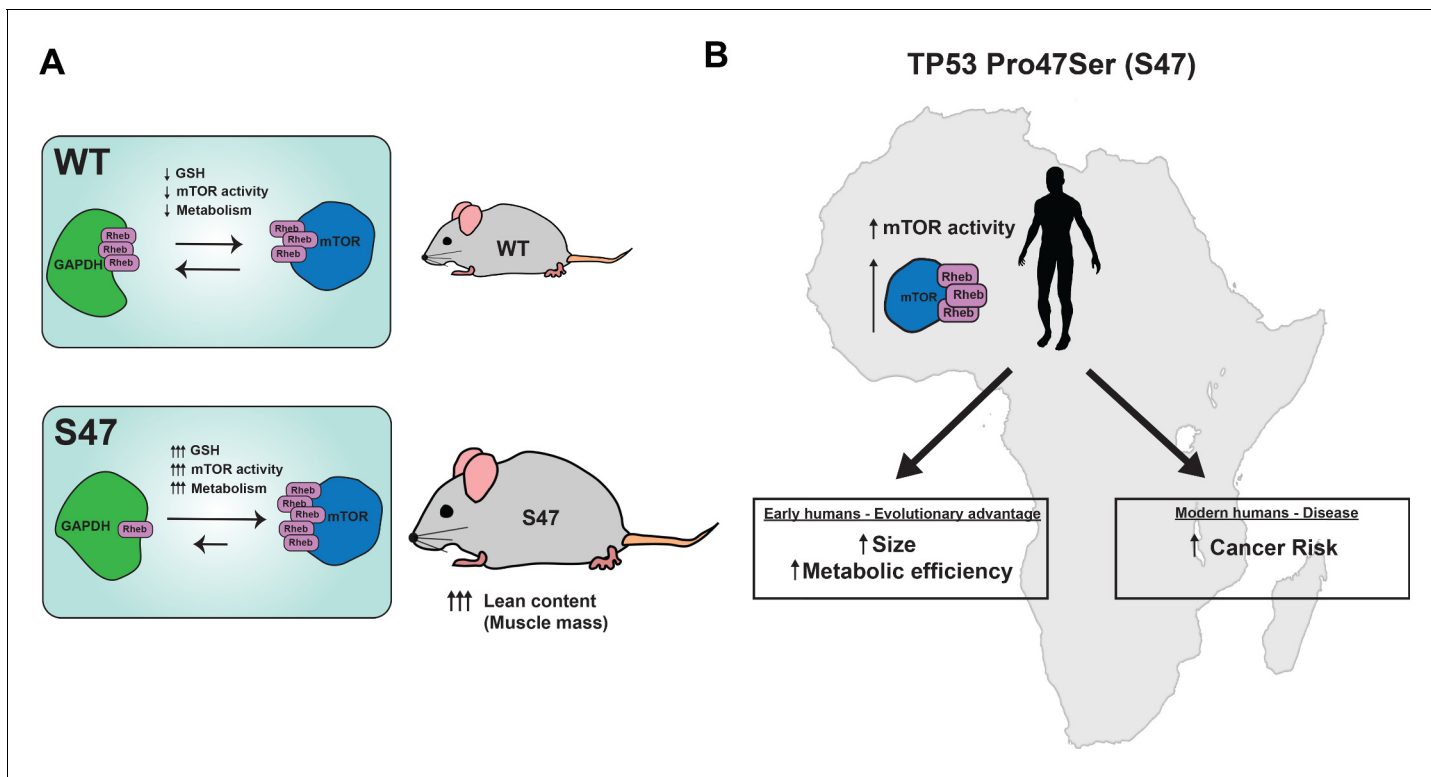


Figure 7. Proposed model. (A) Proposed model of how S47 contributes to increased metabolism. The elevated levels of GSH alter the redox state of the S47 cell, in turn affecting GAPDH conformation and impairing GAPDH-Rheb binding. This results in increased mTOR-Rheb binding, leading to increased mTOR activity and resulting an overall increase in metabolism in S47 mice, as seen by increased fat and lean content. (B) Broad impact of S47 variant: although providing an adaptive advantage to individuals residing in sub-Saharan Africa at one point in time, it now predisposes modern humans with this SNP to cancer.

Materials and methods

Key resources table

Reagent type (species) or resource	Designation	Source or reference	Identifiers	Additional information
Strain, strain background (<i>M. musculus</i>)	C57Bl/6; P47/S47 Hupki	Jennis et al., 2016		PMID:27034505
Cell lines (<i>M. musculus</i>)	WT/S47 Primary MEFs	Jennis et al., 2016		PMID:27034505
Cell lines (<i>Homo-sapiens</i>)	WT/S47 LCLs	Coriell Institute	GM18870 GM18871 GM18872	PMID:27034505
Antibody	Anti-phospho-mTOR (Ser2448) (Rabbit polyclonal)	Cell Signaling Technologies	Cat# 2971 RRID:AB_330970	WB (1:1000) IHC (1:100)
Antibody	Anti-mTOR (7C10) (Rabbit monoclonal)	Cell Signaling Technologies	Cat# 2983 RRID:AB_2105622	WB (1:1000) PLA (1:500)

Continued on next page

Continued

Reagent type (species) or resource	Designation	Source or reference	Identifiers	Additional information
Antibody	Anti-phospho-S6K1 (Thr389) (Rabbit polyclonal)	Cell Signaling Technologies	Cat# 9205 RRID:AB_330944	WB (1:1000)
Antibody	Anti-phospho-S6K1 (Thr421) (Rabbit polyclonal)	Thermo Fisher Scientific	Cat# PA5-37733 RRID:AB_2554341	IHC (1:100)
Antibody	Anti-S6K1 (Rabbit polyclonal)	Cell Signaling Technologies	Cat# 9202 RRID:AB_331676	WB (1:1000)
Antibody	Anti-GAPDH (14C10) (Rabbit monoclonal)	Cell Signaling Technologies	Cat# 2118 RRID:AB_561053	WB (1:10,000) PLA (1:1000)
Antibody	Anti-TFAM (Rabbit polyclonal)	Abcam	Cat# ab131607 RRID:AB_11154693	WB (1:2000)
Antibody	Anti-MTCO1 (Mouse monoclonal)	Abcam	Cat# ab14705 RRID:AB_2084810	WB (1:2000)
Antibody	Anti-SDHA (Rabbit polyclonal)	Cell Signaling Technologies	Cat# 5839 RRID:AB_10707493	WB (1:1000)
Antibody	Anti-Tom20 (F10) (Mouse monoclonal)	Santa Cruz Biotechnology	Cat# sc-17764 RRID:AB_628381	WB (1:100)
Antibody	Anti-phospho-Akt (Ser473) (Rabbit monoclonal)	Cell Signaling Technologies	Cat# 4060 RRID:AB_2315049	WB (1:1000)
Antibody	Anti-p62 (Rabbit polyclonal)	Cell Signaling Technologies	Cat# 5114 RRID:AB_10624872	WB (1:1000)
Antibody	Anti-LC3B (D11) (Rabbit monoclonal)	Cell Signaling Technologies	Cat# 3868 RRID:AB_2137707	WB (1:1000)
Antibody	Anti-HSP90 (C45G5) (Rabbit monoclonal)	Cell Signaling Technologies	Cat# 4877S RRID:AB_2233307	WB (1:1000)
Antibody	Anti-Rheb (E1G1R) (Rabbit monoclonal)	Cell Signaling Technologies	Cat# 13879 RRID:AB_2721022	WB (1:1000) IF (1:800)
Antibody	Anti-TSC2 (D93F12) (Rabbit monoclonal)	Cell Signaling Technologies	Cat# 4308 RRID:AB_10547134	WB (1:1000) IF (1:100)
Antibody	Anti-Akt (Rabbit polyclonal)	Cell Signaling Technologies	Cat# 9272 RRID:AB_329827	WB (1:1000)
Antibody	Anti-Deptor (Rabbit polyclonal)	Novus Biologicals	Cat# NBP1-49674 RRID:AB_10011798	WB (1:1000)
Antibody	Anti-phospho-AMPK α (Thr172) (Rabbit monoclonal)	Cell Signaling Technologies	Cat# 2535 RRID:AB_331250	WB (1:1000)

Continued on next page

Continued

Reagent type (species) or resource	Designation	Source or reference	Identifiers	Additional information
Antibody	Anti-Ki67 (D3B5) (Rabbit monoclonal)	Cell Signaling Technologies	Cat# 12202 RRID:AB_2620142	IHC (1:400)
Antibody	Anti-phospho-S6 (Ser235/236) (Rabbit monoclonal)	Cell Signaling Technologies	Cat# 4856 RRID:AB_2181037	WB (1:1000)
Antibody	Anti-S6 (54D2) (Mouse monoclonal)	Cell Signaling Technologies	Cat# 2317 RRID:AB_2238583	WB (1:1000)
Antibody	Anti-Rheb (B-12) (Mouse monoclonal)	Santa Cruz Biotechnology	Cat# sc-271509 RRID:AB_10659102	PLA (1:50) IP (1:20)
Antibody	Anti-phospho-4EBP1 (Ser65) (Rabbit polyclonal)	Cell Signaling Technologies	Cat# 9451 RRID:AB_330947	WB (1:1000)
Antibody	Anti-4EBP1 (53H11) (Rabbit monoclonal)	Cell Signaling Technologies	Cat# 9644 RRID:AB_2097841	WB (1:1000)
Antibody	Anti-p53 (1C12) (Mouse monoclonal)	Cell Signaling Technologies	Cat# 2524 RRID:AB_331743	WB (1:1000)
Antibody	Anti-Sco2 (Rabbit polyclonal)	LS Bio	Cat# LS-C349015	WB (1:500)
Antibody	Anti-LAMP1(H4A3) (Mouse monoclonal)	Santa Cruz Biotechnology	Cat# sc-20011 RRID:AB_626853	IF (1:50)
Antibody	Alexa Fluor 594 AffiniPure Goat Anti-Rabbit IgG (H+L)	Jackson Immuno Research Laboratories	Cat #111-585-144 RRID:AB_2307325	IF (1:100)
Antibody	Alexa Fluor 488 AffiniPure Goat Anti-Mouse IgG (H+L)	Jackson Immuno Research Laboratories	Cat #115-545-062 RRID:AB_2338845	IF (1:100)
Antibody	Peroxidase AffiniPure F(ab') ₂ Goat Anti-Mouse IgG (H+L)	Jackson Immuno Research Laboratories	Cat #115-036-062 RRID:AB_2307346	WB (1:10,000)
Antibody	Peroxidase AffiniPure F(ab') ₂ Goat Anti-Rabbit IgG (H+L)	Jackson Immuno Research Laboratories	Cat #111-036-003 RRID:AB_2337942	WB (1:10,000)
Antibody	Peroxidase AffiniPure F(ab') ₂ Donkey Anti-Rabbit IgG (H+L)	Jackson Immuno Research Laboratories	Cat #711-036-152 RRID:AB_2340590	WB (1:10,000)
Commercial assay or kit	Seahorse XF Cell Mito Stress Kit	Agilent	Part Number: 1037015–100	
Commercial assay or kit	Seahorse XF Glycolytic Rate Assay	Agilent	Part Number: 103344–100	

Continued on next page

Continued

Reagent type (species) or resource	Designation	Source or reference	Identifiers	Additional information
Commercial assay or kit	GSH/GSSG Glo Assay	Promega	Cat# V6611	
Commercial assay or kit	PLA Duolink In Situ Starter Kit	Sigma Aldrich	DUO92101	
Chemical compound, drug	Rapamycin	Sigma Aldrich	R0395; CAS 53123-88-9	
Chemical compound, drug	Torin1	Cayman Chemical	Item No. 10997; CAS 1222998-36-8	
Chemical compound, drug	BMH (bismaleimi dohexane)	Thermo Fisher Scientific	Cat# 22330; CAS 4856-87-5	
Chemical compound, drug	DEM (diethylmaleate)	Sigma Aldrich	D97703; CAS 141-05-9	
Chemical compound, drug	BSO (buthionine sulfoximine)	Cayman Chemical	Item no. 14484; CAS 83730-53-4	
Chemical compound, drug	Erastin	Cayman Chemical	Item no. 17754; CAS 571203-78-6	
Chemical compound, drug	GSH (L-Glutathione)	Sigma Aldrich	Cat# G6013, CAS 70-18-8	
Chemical compound, drug	L-Methionine	Sigma Aldrich	Cat# M9625, CAS 63-68-3	
Chemical compound, drug	L-Glutamine	Thermo Fisher Scientific	Cat# 25030081	
Chemical compound, drug	L-Cystine	Sigma Aldrich	Cat# C6727	
Software, algorithm	ImageJ	NIH	RRID:SCR_003070	
Software, algorithm	GraphPad Prism	GraphPad	RRID:SCR_002798	
Other	Pyruvate-free DMEM	Thermo Fisher Scientific	Cat# 21013024	
Other	Glucose-free DMEM	Thermo Fisher Scientific	Cat# 11966025	
Other	EBSS	Thermo Fisher Scientific	Cat# 24010043	
Other	MEM Vitamin	Thermo Fisher Scientific	Cat# 11120052	
Other	MEM Amino Acids	Thermo Fisher Scientific	Cat# 1130051	

Continued on next page

Continued

Reagent type (species) or resource	Designation	Source or reference	Identifiers	Additional information
Other	HBSS	Thermo Fisher Scientific	Cat# 14025092	
Other	Trypan Blue	Thermo Fisher Scientific	Cat# 15250061	
Other	Protein G Agarose	Thermo Fisher Scientific	Cat# 15920010	
Other	MitoTracker Green	Thermo Fisher Scientific	Cat# M7514	

Mammalian cell culture

All cell lines have been confirmed of identity using STR profiling; most were obtained by the Coriell Institute. All were confirmed to be free of mycoplasma prior to each experiment. WT and S47 MEFs were generated and maintained as previously described (Jennis *et al.*, 2016). Human WT LCLs (Catalog ID GM18870) and S47 LCLs (Catalog ID GM18871) were obtained from the Coriell Institute (Camden, New Jersey) and maintained as previously described (Jennis *et al.*, 2016). MEF cultured cells were grown in DMEM (Corning Cellgro) supplemented with 10% fetal bovine serum (HyClone, GE Healthcare Life Sciences) and 1% penicillin/streptomycin (Corning Cellgro). Human LCLs were grown in RPMI (Corning Cellgro) supplemented with 15% heat inactivated fetal bovine serum (HyClone, GE Healthcare Life Sciences) and 1% penicillin/streptomycin (Corning Cellgro). Cells were grown in a 5% CO₂ humidified incubator at 37°C. For serum starvation experiments, cells were starved in DMEM containing 0.1% FBS for 16 hr. Following starvation, DMEM containing 10% FBS was re-introduced and cells were harvested at 0 min, 10 min, 30 min, 1 hr, 2 hr, and 8 hr after this point. For glucose starvation experiments, cells were starved in glucose-free DMEM (Thermo Fisher Scientific 11966025) for 16 hr. Following starvation, DMEM containing 4.5 g/L glucose was re-introduced and cells were harvested at 0 min, 10 min, 30 min, 1 hr, 2 hr, and 5 hr after this point. For amino acid starvation experiments, cells were starved for 4 hr in EBSS (Thermo Fisher Scientific 24010043) containing 25 mM glucose, 0.5 mM Glutamine, 1X MEM Vitamin (Thermo Fisher Scientific 11120052), 0.2% FBS, 25 mM HEPES, 1X Penicillin/Streptomycin. Following starvation, the same media recipe now containing 1X MEM Amino Acids (Thermo Fisher 1130051) was re-introduced and cells were harvested at 0 min, 10 min, 30 min, 1 hr, 2 hr, and 5 hr after this point. For HBSS experiments, cells were washed once with PBS (Corning 21-031-CV) and then incubated with HBSS (Thermo Fisher Scientific 14025092) for 0, 2, or 6 hr. Viability was assessed using Trypan Blue (Thermo Fisher Scientific 15250061).

Western blot

For western blot analyses, 50–100 µg of protein was resolved over SDS-PAGE gels using 10% NuPAGE Bis-Tris precast gels (Life Technologies) and were then transferred onto polyvinylidene difluoride membranes (IPVH00010, pore size: 0.45 µm; Millipore Sigma). Membranes were blocked for 1 hr in 5% bovine albumin serum (Sigma Aldrich, A9647). The following antibodies were used for western blot analyses: phospho-mTOR 1:1000 (Cell Signaling, 2971), mTOR 1:1000 (7C10, Cell Signaling, 2983), phospho-p70S6K1 1:1000 (Cell Signaling, 9205), p70S6K1 1:1000 (Cell Signaling, 9202), GAPDH 1:10,000 (14C10, Cell Signaling, 2118), TFAM 1:2000 (Abcam, ab131607), MTCO1 1:2000 (Abcam, ab14705), SDHA 1:1000 (Cell Signaling, 5839), Tom20 1:100 (F-10, Santa Cruz, sc17764), phospho-Akt (D9E, Cell Signaling, 4060), p62 1:1000 (Cell Signaling, 5114), LC3B 1:1000 (D11, Cell Signaling, 3868), HSP90 1:1000 (Cell Signaling, 4877S), Rheb 1:1000 (E1G1R, Cell Signaling, 13879), TSC2 1:1000 (D93F12, Cell Signaling, 4308), Akt 1:1000 (Cell Signaling, 9272), Deptor 1:1000 (Novus Bio, NBP1-49674SS), phospho-AMPKα (Cell Signaling, 2535). Rabbit or mouse secondary antibodies conjugated to horseradish peroxidase were used at a 1:10,000 dilution (Jackson

Immunochemicals), followed by a 5-min treatment with ECL (Amersham, RPN2232). Protein levels were detected using autoradiography and densitometry analysis of protein content was conducted using ImageJ software (NIH, Rockville, MD).

Immunohistochemistry

Tissues were harvested and fixed in formalin overnight at 4°C, followed by a wash with 1X PBS and were then placed in 70% ethanol prior to paraffin embedding. The Wistar Institute Histotechnology Facility performed the tissue embedding and sectioning. For the immunohistochemistry (IHC) studies, paraffin embedded tissue sections were de-paraffinized in xylene (Fisher, X5-SK4) and rehydrated in ethanol (100%–95%–85–75%) followed by distilled water. Samples underwent antigen retrieval by steaming slides in 10 mM Citrate Buffer (pH 6). Endogenous peroxidase activity was quenched with 3% hydrogen peroxide and slides were incubated in blocking buffer (Vector Laboratories, S-2012) for 1 hr. The slides were incubated with phospho-p70S6K1 (1:100, ThermoFisher Scientific, PA5-37733) or phospho-mTOR (1:100, Cell Signaling, 2971) primary antibody overnight at 4°C. The following day, slides were washed with PBS and incubated with HRP-conjugated secondary antibody for 30 min. Antibody complexes were detected using DAB chromogen (D5637). Light counterstaining was done with hematoxylin. Slides were imaged using the Nikon 80i upright microscope and at least four fields were taken per section.

Co-immunoprecipitation

Following overnight seeding of WT and S47 immortalized MEFs, the cells were washed with 1X DPBS and the cell culture medium was replaced with 1% FBS DMEM medium [pyruvate-free DMEM (Thermo Fisher Scientific #21013024) supplemented with 1% FBS, 1% penicillin/streptomycin, 0.1 mM L-Methionine, 0.5 mM L-Glutamine, and 0.033 mM L-Cystine]. WT cells were treated with PBS or 3 mM GSH for 24 hr; while the S47 cells were treated with PBS for 5 hr or 24 hr, 100 μM BSO for 24 hr, or 50 μM DEM for 5 hr. Cells were harvested and centrifuged at 500 x g for 10 min at 4°C. The cell pellets were resuspended in CHAPS Lysis Buffer (1X DPBS with 0.3% CHAPS and freshly added protease inhibitors) at 4°C. Cell disruption was performed by passing the cells through a 23-gauge needle attached to a 1 ml syringe. The skeletal muscles were homogenized using the Qiagen Tissue Lyser II. Total cellular homogenates were rotated/nutated at 4°C for 30 min, and spun at 11,000 x g for 20 min at 4°C. Protein extracts (3 mg per reaction) were incubated with the Rheb antibody (Santa Cruz, sc-271509) overnight at 4°C. The Rheb-immunocomplexes were captured using recombinant protein G agarose (Thermo Fisher Scientific, 15920010) at 4°C for 2 hr. Resins were washed three times using the CHAPS Lysis Buffer. Equal volumes of 2x Laemmli Sample Buffer were added to each reaction, samples were heated for 10 min at 100°C. The Rheb-associated proteins were analyzed by western blotting, using GAPDH (Cell Signaling, 2118), Rheb (Cell Signaling, 13879), and mTOR (7C10, Cell Signaling, 2983) antibodies.

Mitochondrial metabolism and mTOR inhibition assays

The oxygen consumption rate (OCR) and glycolytic rate were determined using the Seahorse XF MitoStress Assay and the Seahorse XF Glycolytic Rate Assay, respectively, according to the manufacturer's protocol. Cells were plated one day prior to the assay, LCLs at 100,000 cells/well and MEFs at 60,000 cells/well. LCLs were treated with 200 nM rapamycin, 100 nM Torin1 or 1 μM Torin1 for 24 hr prior to running the MitoStress Assay. To assess differences in mTOR inhibition, WT and S47 LCLs were treated with 200 nM rapamycin or 100 nM Torin1 for 0 min, 10 min, 30 min, 1 hr, 2 hr, or 6 hr and subsequently cells were harvested for western blot analysis. To determine mitochondrial content, WT and S47 MEFs were incubated with 500 nM of MitoTracker Green (ThermoFisher Scientific, M7514) for 1 hr at 37°C. Cells were then spun down, washed once with PBS, spun down and resuspended in PBS. The FACSCelesta (BD Biosciences) was used to detect fluorescence and at least 10,000 events were measured per sample.

Metabolite measurements

Media was collected after 24 hr after plating LCLs or MEFs, and the YSI-71000 Bioanalyzer was used to determine glucose, glutamine, lactate and glutamate levels as previously described (Londoño Gentile *et al.*, 2013). For the metabolic flux studies, cells were incubated in uniformly

labeled ^{13}C -glucose (25 mM) as indicated in the figure legends. For intracellular extracts, after incubation, the culture medium was aspirated and cells were washed once in ice-cold PBS. Metabolites were extracted by adding a solution of methanol/acetonitrile/water (5:3:2) to the well. Plates were incubated at 4°C for 5 min on a rocker and then the extraction solution was collected. The metabolite extract was cleared by centrifuging at 15,000 \times g for 10 min at 4°C. Supernatants were transferred to LC-MS silanized glass vials with PTFE caps and either run immediately on the LC-MS or stored at -80°C . LC-MS analysis was performed on a Q Exactive Hybrid Quadrupole-Orbitrap HF-X MS (ThermoFisher Scientific) equipped with a HESI II probe and coupled to a Vanquish Horizon UHPLC system (ThermoFisher Scientific). 0.002 ml of sample is injected and separated by HILIC chromatography on a ZIC-pHILIC 2.1 mm. Samples were separated by ammonium carbonate, 0.1% ammonium hydroxide, pH 9.2, and mobile phase B is acetonitrile. The LC was run at a flow rate of 0.2 ml/min and the gradient used was as follows: 0 min, 85% B; 2 min, 85% B; 17 min, 20% B; 17.1 min, 85% B; and 26 min, 85% B. The column was maintained at 45°C and the mobile phase was also pre-heated at 45°C before flowing into the column. The relevant MS parameters were as listed: sheath gas, 40; auxiliary gas, 10; sweep gas, 1; auxiliary gas heater temperature, 350°C; spray voltage, 3.5 kV for the positive mode and 3.2 kV for the negative mode. Capillary temperature was set at 325°C, and funnel RF level at 40. Samples were analyzed in full MS scan with polarity switching at scan range 65 to 975 m/z; 120,000 resolution; automated gain control (AGC) target of 1E6; and maximum injection time (max IT) of 100 milliseconds. Identification and quantitation of metabolites was performed using an annotated compound library and TraceFinder 4.1 software. The 'M+X' nomenclature refers to the isotopologue for that given metabolite. Isotopologues are chemically identical metabolites that differ only in their number of carbon-13 atoms. For instance, 'M+two citrate' means that two of the six carbons in citrate are carbon-13 while the other four are carbon-12. 'M+four citrate' means that four of the six carbons in citrate are carbon-13 while the other two are carbon-12. Isotopologue fractional labeling was corrected for carbon-13 natural abundance.

GSH/GSSG abundance and BMH crosslinking

Relative GSH/GSSG abundance was measured using the GSH/GSSG-Glo Assay (Promega catalog #V6611), according to the manufacturer's instruction. Immortalized WT and S47 MEFs were generated and maintained as previously described (Jennis *et al.*, 2016; Leu *et al.*, 2019). For BMH crosslinking studies, the WT and S47 cells were cultured in 1% FBS DMEM medium and treated with PBS or 50 μM diethyl maleate (DEM, ThermoFisher Scientific AC114440010) for 5 hr; PBS or 100 μM BSO (Cayman Chemical item #14484) for 24 hr; or DMSO or 2 μM Erastin (Cayman Chemical item #17754) for 24 hr. Proteins were extracted from cultured cells or mouse tissue (skeletal muscle, lungs) using 1X DPBS (Thermo Fisher Scientific 14190144) supplemented with 0.5% IGEPAL CA-630, 1 mM PMSF, 6 $\mu\text{g}/\text{ml}$ aprotinin, and 6 $\mu\text{g}/\text{ml}$ leupeptin at 4 °C. The tissues were homogenized using the Wheaton Overhead Stirrer. Total cellular homogenates were pulse sonicated using the Branson digital sonifier set at 39% amplitude. Total protein extracts (100 μg per reaction) were incubated with or without 1 mM BMH (Thermo Fisher Scientific 22330) for 30 min at 30°C. The samples were quenched with an equal volume of 2x Laemmli Sample Buffer (BioRad 1610737) supplemented with 5% β -Mercaptoethanol (BioRad 1610710) and heated for 10 min at 100°C. The protein samples were size fractionated on Novex 4–20% Tris-Glycine Mini Gels (Thermo Fisher Scientific XP04200BOX) at room temperature and subsequently transferred overnight onto Immuno-Blot PVDF membranes (BioRad 1620177) at 4°C. The membranes were blocked with 3% nonfat dry milk (BioRad 1706404) in 1X PBST for 30 min at room temperature and incubated with the GAPDH antibody (Cell Signaling Technology 2118) overnight with rotation/nutation at 4°C. After washing the blots in 1X PBST, the membranes were incubated with Donkey anti-Rabbit (Jackson ImmunoResearch 711-036-152) for 2 hr at room temperature. Membrane-immobilized protein detection used ECL western blotting detection reagents (GE Healthcare RPN2106; Millipore Sigma GERPN2106).

Proximity ligation assay

Cells were grown on Lab-Tek II eight-well chamber slides, and were either untreated, treated with 50 μM diethyl maleate (DEM, ThermoFisher Scientific AC114440010) for 5 hr or treated with 10 μM of buthionine sulfoximine for 24 hr (BSO, Cayman Chemicals, 83730-53-4) and fixed with 4% paraformaldehyde (Electron Microscopy Sciences, 15710). Protein-protein interactions were assessed using

the PLA Duolink in situ starter kit (Sigma Aldrich, DUO92101) following the manufacturer's protocol. The following primary antibodies were used: Rheb 1:50 (B-12, Santa Cruz, sc271509), mTOR 1:500 (7C10, Cell Signaling, 2983), GAPDH 1:1000 (14C10, Cell Signaling, 2118). ImageJ software (NIH, Rockville, MD) was used to quantify PLA signals.

Immunofluorescence staining

Cells were fixed in 4% paraformaldehyde for 10 min, followed by 3 PBS washes and then permeabilization with 0.25% Triton X-100 for 10 min. Cells were washed 3x with PBS, blocked for 1 hr in a PBS solution containing 1% bovine serum albumin and 5% normal goat serum (Jackson ImmunoResearch 005-000-121). Cells were incubated overnight at 4°C with the following primary antibodies diluted in blocking buffer: Rheb 1:800 (Cell Signaling Technologies, #13879), TSC2 1:100 (Cell Signaling Technologies, #4308), LAMP1 1:50 (Santa Cruz, sc-20011). Cells were washed with PBS and incubated with the following secondary antibodies at 37°C for 45 min: Alexa Fluor 594 AffiniPure Goat Anti-Rabbit IgG (Jackson ImmunoResearch 111-585-144) and Alexa Fluor 488 AffiniPure Goat Anti-Mouse IgG (Jackson ImmunoResearch 115-545-062). The cells were mounted with media containing DAPI and images were captured using the Leica TSC SP5 microscope.

Body composition and metabolic cage studies

WT and S47 mice in a pure C57Bl/6 background are previously described (*Jennis et al., 2016*). All mouse studies were performed in accordance with the guidelines in the Guide for the Care and Use of Laboratory Animals of the NIH and all protocols were approved by the Wistar Institute Institutional Animal Care and Use Committee (IACUC). Mice were fed an ad libitum diet and were housed in plastic cages with a 12 hr/12 hr light cycle at 22°C unless otherwise stated. Fat and lean content were measured in live male mice at 6 weeks of age using nuclear magnetic resonance (NMR) with the Minispec LF90 (Bruker Biospin, Billerica, MA). Indirect calorimetry was conducted to assess metabolic capabilities in mice (Oxyman/Comprehensive Laboratory Animal Monitoring System (CLAMS); Columbus Instruments). Data for the WT mice was previously published in supplemental data of *Kung et al., 2016*. Six-week-old mice were single caged, provided with water and food ad libitum and allowed to acclimate to the cages for 2 days. Oxygen consumption (VO_2) and carbon dioxide production (VCO_2) were recorded for 48 hr using an air flow of 600 ml/min and temperature of 22°C. Respiratory exchange ratio (RER) is calculated as VCO_2/VO_2 and heat (kcal/h) is calculated by $3.815 + 1.232 \times (\text{RER})$. Photodetectors were used to measure physical activity (Optovarimex System; Columbus Instruments).

Treadmill and serum metabolite studies

Mice were allowed to acclimate to the metabolic treadmill (Columbus Instruments) for 5 min before beginning their runs. The treadmill was then set to 5 m/min and speed increased by 5 m/min every 2 min until 20 m/min was reached. Upon reaching 20 m/min, the incline was increased by 5° every 2 min until reaching a maximum of 25 degrees. Mice were allowed to run at this maximum speed and incline until exhaustion, defined by the mice spending 10 continuous seconds on the shock grid. Lactate (Nova Biomedical) and glucose (One Touch) measurements were taken using test strips just prior to treadmill entry and immediately after exhaustion using handheld meters. Tail blood was also taken prior to treadmill entry and immediately after exhaustion and metabolites measured using the Vettester serum analyzer (Idexx Laboratories).

Statistical analysis

Unless otherwise stated, all experiments were performed in triplicate. The two-tailed unpaired Student t-test was performed. All in vitro data are reported as the mean \pm SD unless stated otherwise, and in vivo are reported as the mean \pm SE. Statistical analyses were performed using GraphPad Prism, p-values are as follows: (*) p-value < 0.05, (**) p-value < 0.01, (***) p-value < 0.001, (****) p-value < 0.0001. For the CLAMs and mouse exercise data, the Wilcoxon rank-sum test was used to compare the differences between S47 and WT mice.

Acknowledgements

This work was supported by R01 CA102184 (MEM), R01 CA139319 (DLG and MEM), R01 CA238611 (MEM), P01 CA114046 (DLG and MEM), T32 CA009071, F32 CA220972 and K99 CA241367 (TB), R01 CA174761 (KEW), R01 AG043483 and DK098656 (JAB) and the Rodent Metabolic Phenotyping Core (P30-DK19525), and DP2-CA249951 (ZTS). RSA is partly supported by a Bloomberg Distinguished Professorship. The authors acknowledge the Histotechnology, Laboratory Animal and Imaging facilities at the Wistar Institute. The authors are grateful to Allie Lipshutz and Lindsey Schweitzer for expert technical help, and Matthew Jennis for the mouse weight data.

Additional information

Competing interests

Maureen E Murphy: Senior Editor, eLife. The other authors declare that no competing interests exist.

Funding

Funder	Grant reference number	Author
National Cancer Institute	R01 CA102184	Maureen E Murphy
National Cancer Institute	R01 CA139319	Donna L George Maureen E Murphy
National Cancer Institute	CA238611	Maureen E Murphy
National Cancer Institute	P01 CA114046	Donna L George Maureen E Murphy
National Cancer Institute	T32 CA009171	Thibaut Barnoud
National Cancer Institute	F32 CA220972	Thibaut Barnoud
National Cancer Institute	K99 CA241367	Thibaut Barnoud
National Cancer Institute	R01 CA174761	Kathryn E Wellen
National Institute on Aging	R01 AG043483	Joseph A Baur
National Institute of Diabetes and Digestive and Kidney Diseases	R01 DK098656	Joseph A Baur
National Institute of Diabetes and Digestive and Kidney Diseases	P30 DK19525	Joseph A Baur
National Cancer Institute	DP2-CA249951	Zachary T Schug
Bloomberg Family Foundation		Rexford Ahima
National Cancer Institute	Cancer Center Support Grant (CCSG) P30 CA010815	Maureen E Murphy

The funders had no role in study design, data collection and interpretation, or the decision to submit the work for publication.

Author contributions

Keerthana Gnanapradeepan, Conceptualization, Formal analysis, Validation, Investigation, Visualization, Methodology, Writing - original draft, Writing - review and editing; Julia I-Ju Leu, Conceptualization, Formal analysis, Investigation, Methodology, Writing - review and editing; Subhasree Basu, Conceptualization, Formal analysis, Investigation, Writing - review and editing; Thibaut Barnoud, Conceptualization, Formal analysis, Funding acquisition, Investigation, Writing - review and editing; Madeline Good, Formal analysis, Investigation; Joyce V Lee, William J Quinn, Che-Pei Kung, Data curation, Formal analysis, Investigation, Writing - review and editing; Rexford Ahima, Joseph A Baur, Kathryn E Wellen, Data curation, Funding acquisition, Methodology, Writing - review and editing;

Qin Liu, Formal analysis, Methodology, Writing - review and editing; Zachary T Schug, Data curation, Formal analysis, Funding acquisition, Investigation, Methodology, Writing - review and editing; Donna L George, Funding acquisition, Methodology, Writing - review and editing; Maureen E Murphy, Conceptualization, Formal analysis, Funding acquisition, Writing - review and editing

Author ORCIDs

Keerthana Gnanapradeepan  <https://orcid.org/0000-0002-8984-9742>

Thibaut Barnoud  <http://orcid.org/0000-0001-5588-6281>

Che-Pei Kung  <http://orcid.org/0000-0002-1150-4998>

Joseph A Baur  <http://orcid.org/0000-0001-8262-6549>

Kathryn E Wellen  <https://orcid.org/0000-0002-2281-0042>

Maureen E Murphy  <https://orcid.org/0000-0001-7644-7296>

Ethics

Animal experimentation: This study was performed in strict accordance with the recommendations in the Guide for the Care and Use of Laboratory Animals of the National Institutes of Health. All of the animals were handled according to approved institutional animal care and use committee (IACUC) protocols of the University of Pennsylvania (protocol 804474) and The Wistar Institute (protocol 201283).

Decision letter and Author response

Decision letter <https://doi.org/10.7554/eLife.55994.sa1>

Author response <https://doi.org/10.7554/eLife.55994.sa2>

Additional files

Supplementary files

- Transparent reporting form

Data availability

All data generated or analysed during this study are included in the manuscript and supporting files. Source data files are provided for Figure 6 and Figure 2—figure supplement 1.

References

- Baar EL, Carbajal KA, Ong IM, Lamming DW. 2016. Sex- and tissue-specific changes in mTOR signaling with age in C57BL/6J mice. *Aging Cell* **15**:155–166. DOI: <https://doi.org/10.1111/ace.12425>, PMID: 26695882
- Basu S, Gnanapradeepan K, Barnoud T, Kung CP, Tavecchio M, Scott J, Watters A, Chen Q, Kossenkov AV, Murphy ME. 2018. Mutant p53 controls tumor metabolism and metastasis by regulating PGC-1 α . *Genes & Development* **32**:230–243. DOI: <https://doi.org/10.1101/gad.309062.117>, PMID: 29463573
- Ben-Sahra I, Manning BD. 2017. mTORC1 signaling and the metabolic control of cell growth. *Current Opinion in Cell Biology* **45**:72–82. DOI: <https://doi.org/10.1016/j.ceb.2017.02.012>, PMID: 28411448
- Berkers CR, Maddocks OD, Cheung EC, Mor I, Vousden KH. 2013. Metabolic regulation by p53 family members. *Cell Metabolism* **18**:617–633. DOI: <https://doi.org/10.1016/j.cmet.2013.06.019>, PMID: 23954639
- Brandes N, Schmitt S, Jakob U. 2009. Thiol-based redox switches in eukaryotic proteins. *Antioxidants & Redox Signaling* **11**:997–1014. DOI: <https://doi.org/10.1089/ars.2008.2285>, PMID: 18999917
- Budanov AV, Karin M. 2008. p53 target genes sestrin1 and sestrin2 connect genotoxic stress and mTOR signaling. *Cell* **134**:451–460. DOI: <https://doi.org/10.1016/j.cell.2008.06.028>, PMID: 18692468
- Chernorizov KA, Elkina JL, Semenyuk PI, Svedas VK, Mironetz VI. 2010. Novel inhibitors of glyceraldehyde-3-phosphate dehydrogenase: covalent modification of NAD-binding site by aromatic thiols. *Biochemistry. Biokhimiia* **75**:1444–1449. DOI: <https://doi.org/10.1134/s0006297910120047>, PMID: 21314614
- Coleman ME, DeMayo F, Yin KC, Lee HM, Geske R, Montgomery C, Schwartz RJ. 1995. Myogenic vector expression of insulin-like growth factor I stimulates muscle cell differentiation and myofiber hypertrophy in transgenic mice. *Journal of Biological Chemistry* **270**:12109–12116. DOI: <https://doi.org/10.1074/jbc.270.20.12109>, PMID: 7744859

- Dickinson JM**, Rasmussen BB. 2011. Essential amino acid sensing, signaling, and transport in the regulation of human muscle protein metabolism. *Current Opinion in Clinical Nutrition and Metabolic Care* **14**:83–88. DOI: <https://doi.org/10.1097/MCO.0b013e3283406f3e>, PMID: 21076294
- Drummond MJ**, Fry CS, Glynn EL, Dreyer HC, Dhanani S, Timmerman KL, Volpi E, Rasmussen BB. 2009. Rapamycin administration in humans blocks the contraction-induced increase in skeletal muscle protein synthesis. *The Journal of Physiology* **587**:1535–1546. DOI: <https://doi.org/10.1113/jphysiol.2008.163816>, PMID: 19188252
- Fang Y**, Westbrook R, Hill C, Boparai RK, Arum O, Spong A, Wang F, Javors MA, Chen J, Sun LY, Bartke A. 2013. Duration of rapamycin treatment has differential effects on metabolism in mice. *Cell Metabolism* **17**:456–462. DOI: <https://doi.org/10.1016/j.cmet.2013.02.008>, PMID: 23473038
- Feng Z**, Zhang H, Levine AJ, Jin S. 2005. The coordinate regulation of the p53 and mTOR pathways in cells. *PNAS* **102**:8204–8209. DOI: <https://doi.org/10.1073/pnas.0502857102>, PMID: 15928081
- Feng Z**, Hu W, de Stanchina E, Teresky AK, Jin S, Lowe S, Levine AJ. 2007. The regulation of AMPK beta1, TSC2, and PTEN expression by p53: stress, cell and tissue specificity, and the role of these gene products in modulating the IGF-1-AKT-mTOR pathways. *Cancer Research* **67**:3043–3053. DOI: <https://doi.org/10.1158/0008-5472.CAN-06-4149>, PMID: 17409411
- Gnanapradeepan K**, Basu S, Barnoud T, Budina-Kolomets A, Kung CP, Murphy ME. 2018. The p53 tumor suppressor in the control of metabolism and ferroptosis. *Frontiers in Endocrinology* **9**:124. DOI: <https://doi.org/10.3389/fendo.2018.00124>, PMID: 29695998
- Goodman CA**. 2019. Role of mTORC1 in mechanically induced increases in translation and skeletal muscle mass. *Journal of Applied Physiology* **127**:581–590. DOI: <https://doi.org/10.1152/jappphysiol.01011.2018>, PMID: 30676865
- Green NS**, Reisler E, Houk KN. 2001. Quantitative evaluation of the lengths of homobifunctional protein cross-linking reagents used as molecular rulers. *Protein Science* **10**:1293–1304. DOI: <https://doi.org/10.1110/ps.51201>
- Hasty P**, Sharp ZD, Curiel TJ, Campisi J. 2013. mTORC1 and p53: clash of the gods? *Cell Cycle* **12**:20–25. DOI: <https://doi.org/10.4161/cc.22912>, PMID: 23255104
- Hollstein M**, Sidransky D, Vogelstein B, Harris CC. 1991. p53 mutations in human cancers. *Science* **253**:49–53. DOI: <https://doi.org/10.1126/science.1905840>, PMID: 1905840
- Jennis M**, Kung CP, Basu S, Budina-Kolomets A, Leu JI, Khaku S, Scott JP, Cai KQ, Campbell MR, Porter DK, Wang X, Bell DA, Li X, Garlick DS, Liu Q, Hollstein M, George DL, Murphy ME. 2016. An African-specific polymorphism in the TP53 gene impairs p53 tumor suppressor function in a mouse model. *Genes & Development* **30**:918–930. DOI: <https://doi.org/10.1101/gad.275891.115>, PMID: 27034505
- Jung CH**, Ro SH, Cao J, Otto NM, Kim DH. 2010. mTOR regulation of autophagy. *FEBS Letters* **584**:1287–1295. DOI: <https://doi.org/10.1016/j.febslet.2010.01.017>, PMID: 20083114
- Kang HJ**, Feng Z, Sun Y, Atwal G, Murphy ME, Rebbeck TR, Rosenwaks Z, Levine AJ, Hu W. 2009. Single-nucleotide polymorphisms in the p53 pathway regulate fertility in humans. *PNAS* **106**:9761–9766. DOI: <https://doi.org/10.1073/pnas.0904280106>, PMID: 19470478
- Kung CP**, Leu JI, Basu S, Khaku S, Anokye-Danso F, Liu Q, George DL, Ahima RS, Murphy ME. 2016. The P72R polymorphism of p53 predisposes to obesity and metabolic dysfunction. *Cell Reports* **14**:2413–2425. DOI: <https://doi.org/10.1016/j.celrep.2016.02.037>, PMID: 26947067
- Laplante M**, Sabatini DM. 2012. mTOR signaling in growth control and disease. *Cell* **149**:274–293. DOI: <https://doi.org/10.1016/j.cell.2012.03.017>, PMID: 22500797
- Lee MN**, Ha SH, Kim J, Koh A, Lee CS, Kim JH, Jeon H, Kim DH, Suh PG, Ryu SH. 2009. Glycolytic flux signals to mTOR through glyceraldehyde-3-phosphate dehydrogenase-mediated regulation of rheb. *Molecular and Cellular Biology* **29**:3991–4001. DOI: <https://doi.org/10.1128/MCB.00165-09>, PMID: 19451232
- Leu JI**, Murphy ME, George DL. 2019. Mechanistic basis for impaired ferroptosis in cells expressing the African-centric S47 variant of p53. *PNAS* **116**:8390–8396. DOI: <https://doi.org/10.1073/pnas.1821277116>, PMID: 30962386
- Liu GY**, Sabatini DM. 2020. mTOR at the nexus of nutrition, growth, ageing and disease. *Nature Reviews Molecular Cell Biology* **21**:183–203. DOI: <https://doi.org/10.1038/s41580-019-0199-y>, PMID: 31937935
- Londoño Gentile T**, Lu C, Lodato PM, Tse S, Olejniczak SH, Witze ES, Thompson CB, Wellen KE. 2013. DNMT1 is regulated by ATP-citrate lyase and maintains methylation patterns during adipocyte differentiation. *Molecular and Cellular Biology* **33**:3864–3878. DOI: <https://doi.org/10.1128/MCB.01495-12>, PMID: 23897429
- Long X**, Lin Y, Ortiz-Vega S, Yonezawa K, Avruch J. 2005. Rheb binds and regulates the mTOR kinase. *Current Biology* **15**:702–713. DOI: <https://doi.org/10.1016/j.cub.2005.02.053>, PMID: 15854902
- Morita M**, Gravel SP, Chénard V, Sikström K, Zheng L, Alain T, Gandin V, Avizonis D, Arguello M, Zakaria C, McLaughlan S, Nouet Y, Pause A, Pollak M, Gottlieb E, Larsson O, St-Pierre J, Topisirovic I, Sonenberg N. 2013. mTORC1 controls mitochondrial activity and biogenesis through 4E-BP-dependent translational regulation. *Cell Metabolism* **18**:698–711. DOI: <https://doi.org/10.1016/j.cmet.2013.10.001>, PMID: 24206664
- Murphy ME**, Liu S, Yao S, Huo D, Liu Q, Dolfi SC, Hirshfield KM, Hong CC, Hu Q, Olshan AF, Ogundiran TO, Adebamowo C, Domchek SM, Nathanson KL, Nemesure B, Ambs S, Blot WJ, Feng Y, John EM, Bernstein L, et al. 2017. A functionally significant SNP in TP53 and breast Cancer risk in African-American women. *Npj Breast Cancer* **3**:5. DOI: <https://doi.org/10.1038/s41523-017-0007-9>, PMID: 28649645
- Musarò A**, McCullagh K, Paul A, Houghton L, Dobrowolny G, Molinaro M, Barton ER, Sweeney HL, Rosenthal N. 2001. Localized Igf-1 transgene expression sustains hypertrophy and regeneration in senescent skeletal muscle. *Nature Genetics* **27**:195–200. DOI: <https://doi.org/10.1038/84839>, PMID: 11175789

- Schieke SM**, Phillips D, McCoy JP, Aponte AM, Shen RF, Balaban RS, Finkel T. 2006. The mammalian target of rapamycin (mTOR) pathway regulates mitochondrial oxygen consumption and oxidative capacity. *Journal of Biological Chemistry* **281**:27643–27652. DOI: <https://doi.org/10.1074/jbc.M603536200>, PMID: 16847060
- Singh KS**, Leu J, Barnoud T, Vonteddu P, Gnanapradeepan K, Lin C, Liu Q, Barton JC, Kossenkov AV, George DL, Murphy ME, Dotiwala F. 2020. African-centric TP53 variant increases iron accumulation and bacterial pathogenesis but improves response to malaria toxin. *Nature Communications* **11**:473. DOI: <https://doi.org/10.1038/s41467-019-14151-9>, PMID: 31980600
- Smith KR**, Hanson HA, Mineau GP, Buys SS. 2012. Effects of *BRCA1* and *BRCA2* mutations on female fertility. *Proceedings of the Royal Society B: Biological Sciences* **279**:1389–1395. DOI: <https://doi.org/10.1098/rspb.2011.1697>
- Song Z**, Moore DR, Hodson N, Ward C, Dent JR, O’Leary MF, Shaw AM, Hamilton DL, Sarkar S, Gangloff YG, Hornberger TA, Spriet LL, Heigenhauser GJ, Philp A. 2017. Resistance exercise initiates mechanistic target of rapamycin (mTOR) translocation and protein complex co-localisation in human skeletal muscle. *Scientific Reports* **7**:5028. DOI: <https://doi.org/10.1038/s41598-017-05483-x>, PMID: 28694500
- Stockwell BR**, Friedmann Angeli JP, Bayir H, Bush AI, Conrad M, Dixon SJ, Fulda S, Gascón S, Hatzios SK, Kagan VE, Noel K, Jiang X, Linkermann A, Murphy ME, Overholtzer M, Oyagi A, Pagnussat GC, Park J, Ran Q, Rosenfeld CS, et al. 2017. Ferroptosis: a regulated cell death nexus linking metabolism, redox biology, and disease. *Cell* **171**:273–285. DOI: <https://doi.org/10.1016/j.cell.2017.09.021>, PMID: 28985560
- Vandenburg HH**, Karlisch P, Shansky J, Feldstein R. 1991. Insulin and IGF-I induce pronounced hypertrophy of skeletal myofibers in tissue culture. *American Journal of Physiology-Cell Physiology* **260**:C475–C484. DOI: <https://doi.org/10.1152/ajpcell.1991.260.3.C475>
- Vicens A**, Posada D. 2018. Selective pressures on human Cancer genes along the evolution of mammals. *Genes* **9**:582. DOI: <https://doi.org/10.3390/genes9120582>
- Vousden KH**, Prives C. 2009. Blinded by the light: the growing complexity of p53. *Cell* **137**:413–431. DOI: <https://doi.org/10.1016/j.cell.2009.04.037>, PMID: 19410540
- Walton ZE**, Patel CH, Brooks RC, Yu Y, Ibrahim-Hashim A, Riddle M, Porcu A, Jiang T, Ecker BL, Tameire F, Koumenis C, Weeraratna AT, Welsh DK, Gillies R, Alwine JC, Zhang L, Powell JD, Dang CV. 2018. Acid suspends the circadian clock in hypoxia through inhibition of mTOR. *Cell* **174**:72–87. DOI: <https://doi.org/10.1016/j.cell.2018.05.009>
- Wang PY**, Ma W, Park JY, Celi FS, Arena R, Choi JW, Ali QA, Tripodi DJ, Zhuang J, Lago CU, Strong LC, Talagala SL, Balaban RS, Kang JG, Hwang PM. 2013. Increased oxidative metabolism in the Li-Fraumeni syndrome. *New England Journal of Medicine* **368**:1027–1032. DOI: <https://doi.org/10.1056/NEJMoa1214091>, PMID: 23484829
- White EJ**, Martin V, Liu JL, Klein SR, Piya S, Gomez-Manzano C, Fueyo J, Jiang H. 2011. Autophagy regulation in Cancer development and therapy. *American Journal of Cancer Research* **1**:362–372. PMID: 21969237
- Yang YP**, Liang ZQ, Gu ZL, Qin ZH. 2005. Molecular mechanism and regulation of autophagy1. *Acta Pharmacologica Sinica* **26**:1421–1434. DOI: <https://doi.org/10.1111/j.1745-7254.2005.00235.x>, PMID: 16297339
- Ye L**, Varamini B, Lamming DW, Sabatini DM, Baur JA. 2012. Rapamycin has a biphasic effect on insulin sensitivity in C2C12 myotubes due to sequential disruption of mTORC1 and mTORC2. *Frontiers in Genetics* **3**:177. DOI: <https://doi.org/10.3389/fgene.2012.00177>, PMID: 22973301
- Ye L**, Widlund AL, Sims CA, Lamming DW, Guan Y, Davis JG, Sabatini DM, Harrison DE, Vang O, Baur JA. 2013. Rapamycin doses sufficient to extend lifespan do not compromise muscle mitochondrial content or endurance. *Aging* **5**:539–550. DOI: <https://doi.org/10.18632/aging.100576>, PMID: 23929887
- Yoon MS**. 2017. mTOR as a key regulator in maintaining skeletal muscle mass. *Frontiers in Physiology* **8**:788. DOI: <https://doi.org/10.3389/fphys.2017.00788>, PMID: 29089899
- Zhao Y**, Wu L, Yue X, Zhang C, Wang J, Li J, Sun X, Zhu Y, Feng Z, Hu W. 2018. A polymorphism in the tumor suppressor p53 affects aging and longevity in mouse models. *eLife* **7**:e34701. DOI: <https://doi.org/10.7554/eLife.34701>, PMID: 29557783